Petroleum Science 23 (2026) 5319–5333

Contents lists available at ScienceDirect

Petroleum Science

journal homepage: www.keaipublishing.com/en/journals/petroleum-science

Original Paper

Differential inorganic–organic porosity evolution in the Wufeng–Longmaxi Shale, southern Sichuan Basin, China

Guang-Shun Xiao [a,b], Neng-Wu Zhou [c,*], Qin-Hong Hu [a,b], Sheng-Xian Zhao [d], Bo Li [d], Bo Song [a], Xin-Yu Jiang [a], Zi-Yi Wang [c], Shuang-Fang Lu [c,**]

[a] School of Geosciences, China University of Petroleum (East China), Qingdao, 266580, Shandong, China
[b] State Key Laboratory of Deep Oil and Gas, China University of Petroleum (East China), Qingdao, 266580, Shandong, China
[c] Sanya Offshore Oil & Gas Research Institute of Northeast Petroleum University, Sanya, 572025, Hainan, China
[d] Shale Gas Institute of PetroChina Southwest Oil & Gasfield Company, Chengdu, 610051, Sichuan, China

A R T I C L E I N F O

Article history:
Received 22 October 2025
Received in revised form
12 April 2026
Accepted 30 June 2026
Available online 4 July 2026

Edited by Xiu-Fang Hu

Keywords:
Wufeng–Longmaxi Formation
Inorganic–organic porosity
In situ porosity
Quantitative evolution

A B S T R A C T

Quantifying how inorganic and organic porosity co-evolve in shale during burial and later uplift is a key scientific issue for constraining shale-gas occurrence, storage capacity, and enrichment mechanisms. Despite extensive studies, major uncertainties remain regarding (1) quantitatively separating compaction-driven inorganic pore loss from maturity-controlled organic pore generation and (2) restoring porosity under in situ effective stress through geological time. Here we develop an integrated quantitative framework for the Wufeng–Longmaxi shale gas reservoirs in the southern Sichuan Basin, China. Core samples from production wells, in which porosity is primarily controlled by total organic carbon (TOC), were selected to minimize the interference of mineral composition and compaction heterogeneity. Using a TOC–porosity-intercept approach, inorganic porosity was calculated from the intercept of the porosity–TOC linear relationship and its burial evolution was reconstructed with a compaction model constrained by well burial histories. Organic porosity was quantified by extracting organic-matter surface porosity from field-emission scanning electron microscopy (FE-SEM) images using ImageJ, and a maturity-dependent organic porosity evolution model was established from samples spanning different thermal maturities. Total porosity evolution in the Luzhou, Changning, Weiyuan, and Western Chongqing blocks was reconstructed by integrating the inorganic- and organic-porosity models, and in situ porosity was further restored using pressure-confined porosity experiments. Results indicate that inorganic porosity decreases sharply with burial depth, from an initial value of ~50% to 2.47%–4.05% at maximum burial, mainly controlled by mechanical compaction. Organic porosity increases after entering the hydrocarbon generation window and peaks at 1.54%–1.79%, reflecting pore generation during organic matter transformation. Consequently, total porosity declines to 4.16%–5.76% with increasing burial depth, demonstrating that compaction outweighs hydrocarbon-generation-related porosity creation. Restored in situ porosity fluctuates slightly during subsidence but exhibits an overall decreasing trend, reaching 2.34%–3.78% at maximum burial, and then shows only a modest rebound during late-stage tectonic uplift to 2.49%–4.17% at present. Uncertainties are quantified via bootstrap/Monte Carlo propagation and reported as 95% prediction intervals. These results highlight the coupled controls of compaction, hydrocarbon generation, and tectonic unloading on shale pore evolution and provide a quantitative basis for predicting the distribution of high-quality shale reservoirs.

1. Introduction

Understanding the coupled evolution of inorganic and organic porosity in shale reservoirs is fundamental to elucidating shale-gas occurrence, evaluating reservoir quality, and constraining hydrocarbon accumulation and enrichment mechanisms (Loucks et al., 2009; Milliken et al., 2013; Tang et al., 2025). Theoretically,

* Corresponding author.
** Corresponding author.
E-mail addresses: zhounengwu@nepu.edu.cn (N.-W. Zhou), lushuangfang@upc.edu.cn (S.-F. Lu).
Peer review under the responsibility of China University of Petroleum (Beijing).

https://doi.org/10.1016/j.petsci.2026.06.058
1995-8226/

shale porosity is governed by the coupled effects of sedimentation and diagenesis (Athy, 1930; Curtis et al., 2012; Hedberg, 1936; Kuila et al., 2014). During sedimentation, initial porosity is governed by particle attributes such as grain size, roundness, and sorting. During diagenesis, mechanical compaction, mineral precipitation and dissolution, and hydrocarbon generation from organic matter collectively increase or decrease reservoir porosity (Dong et al., 2026; Emmanuel et al., 2010; Mathia et al., 2016; Navarre-Sitchler et al., 2009; Neuhoff et al., 1999; Pommer and Milliken, 2015; Stack et al., 2014; Wang et al., 2024). Consequently, shales with varying sedimentary compositions exhibit pronounced porosity differences during diagenetic evolution, resulting in significant heterogeneity in reservoir space types and their proportions (Zhou et al., 2024). This heterogeneous pore structure markedly affects the gas–water occurrence states within shales. For instance, clay mineral pores primarily contain bound water (Zhang and Liu, 2021), while organic matter pores typically host both adsorbed and free gas (Sang et al., 2016). This suggests that even at identical total porosity values, the spatial heterogeneity in gas content can be substantial due to variations in the proportions of organic and inorganic porosity. Therefore, quantitatively reconstructing the dynamic evolution of organic, inorganic, and total porosity throughout the geological history of shale reservoirs can significantly advance our understanding of shale gas occurrence mechanisms and reservoir performance. It also possesses considerable theoretical and practical importance for deciphering shale gas accumulation processes, predicting gas content, and identifying favorable zones for exploration.

Current approaches for evaluating shale porosity evolution through geological time can be grouped into four main categories: (1) Porosity evolution inferred from simulation experiments. This approach includes two primary methodologies: one involves conducting burial simulation experiments on modern lake or marine sediments under controlled temperature and pressure conditions (Bei and Wang, 1985; Chen and Tian, 1989), focusing on the effects of mechanical compaction on inorganic porosity; the other employs thermal maturation experiments on low-maturity shale (Chen et al., 2025; Hu et al., 2024; Xu et al., 2025), aimed at assessing porosity changes resulting from hydrocarbon generation by organic matter. However, it is often difficult to fully replicate in situ geological conditions, such as temperature, pressure, and time scale, in laboratory settings, leading to significant discrepancies between experimental results and actual observations. For example, deeply buried (>2500 m), highly mature shales in the Sichuan Basin and the southern North China Basin exhibit average porosities of 3.02% (Zou et al., 2010) and 2.8% (Yang and Guo, 2020a), respectively, whereas simulation experiments typically yield porosity values exceeding 4% (Chen and Xiao, 2014; Guo and Mao, 2019; Xie et al., 2014). These inconsistencies highlight the limitations of experimental simulations in quantitatively characterizing porosity evolution. (2) Porosity evolution inferred from natural shale samples at varying depths and maturities. This method analyzes trends in porosity or density differences across different burial depths and thermal maturity levels (Athy, 1930; Baldwin and Butler, 1985; Dzevanshir et al., 1986; Puttiwongrak et al., 2020). While effective in revealing general trends in total porosity evolution under broad compaction regimes, it often overlooks compositional heterogeneity and the complex impacts of late diagenetic processes (e.g., hydrocarbon generation and dissolution). Consequently, its ability to elucidate the underlying mechanisms of porosity evolution remains limited. (3) Porosity evolution inferred through mass-balance calculations based on kerogen volume reduction during hydrocarbon generation (Chen and Jiang, 2016; Chen et al., 2014). This approach focuses primarily on changes in organic porosity but fails to account for pore volume occupied by heavy hydrocarbons, such as bitumen, thereby introducing potential inaccuracies. (4) Porosity evolution determined through microscopic quantification of porosity changes associated with specific diagenetic processes (e.g., dissolution, cementation, hydrocarbon generation), integrated with diagenetic sequences and compaction curves. Theoretically, this method is scientifically robust and has been widely applied in sandstone studies (Bello et al., 2022; Lin et al., 2026; Zhang et al., 2023; Zhou et al., 2023). However, due to the inherently low porosity, fine grain size, and compositional complexity of shales, precise identification of diagenetic types, accurate determination of their timing, and quantitative estimation of their impact on porosity remain challenging. These limitations currently restrict the method's applicability and accuracy in studies of shale porosity evolution.

The dynamic evolution of shale porosity over geological history remains a central challenge in petroleum exploration. Although significant efforts have been devoted to assessing shale porosity, a universally accepted scientific evaluation framework has yet to be established. This study focuses on the Wufeng–Longmaxi shale formation in the southern Sichuan Basin. Based on extensive porosity measurements from shale-gas wells and TOC data, we propose a quantitative approach based on the TOC–porosity relationship to constrain inorganic porosity and reconstruct its evolution. In addition, using field emission scanning electron microscopy (FE-SEM) images of shale samples at varying maturation stages, we established a systematic model for organic porosity evolution. Furthermore, pressure-confined porosity experiments were used to calibrate the effective-stress correction and thereby restore in situ porosity through geological time.

This study systematically examines four shale gas blocks, Luzhou, Changning, Weiyuan, and Western Chongqing, in southern Sichuan to address the following critical scientific questions.

(1) How can quantitative evolution models of total, inorganic, and organic porosity be established for the Wufeng–Longmaxi shale reservoirs in southern Sichuan?
(2) How did total, inorganic, and organic porosity evolve through geological time in the Wufeng–Longmaxi shales of southern Sichuan?
(3) What differences in total, inorganic, and organic porosity exist among the Luzhou, Changning, Weiyuan, and Western Chongqing blocks, and what controls these differences?

By addressing these questions, this study not only advances the theoretical understanding of the interplay between inorganic and organic porosity and their collective impact on porosity evolution, but also offers new scientific insights into shale gas occurrence, reservoir behavior, and accumulation mechanisms. The findings provide critical theoretical support for shale gas exploration in the southern Sichuan Basin, while also delivering valuable references and implications for both emerging and established shale gas plays worldwide.

2. Geological background

The Sichuan Basin, located on the southwestern Yangtze Block, has undergone multiple major tectonic events throughout its geological history, including the Caledonian, Hercynian, Indosinian, Yanshanian, and Himalayan movements, resulting in a complex history of sedimentation and tectonic evolution (Hao et al., 2008; Shi et al., 2024; Tang et al., 2021). Southern Sichuan lies in the southern part of the Sichuan Basin (Guo et al., 2020; Huang et al., 2012) and includes four principal study blocks: Luzhou, Changning, Weiyuan, and Western Chongqing (Fig. 1(a)).

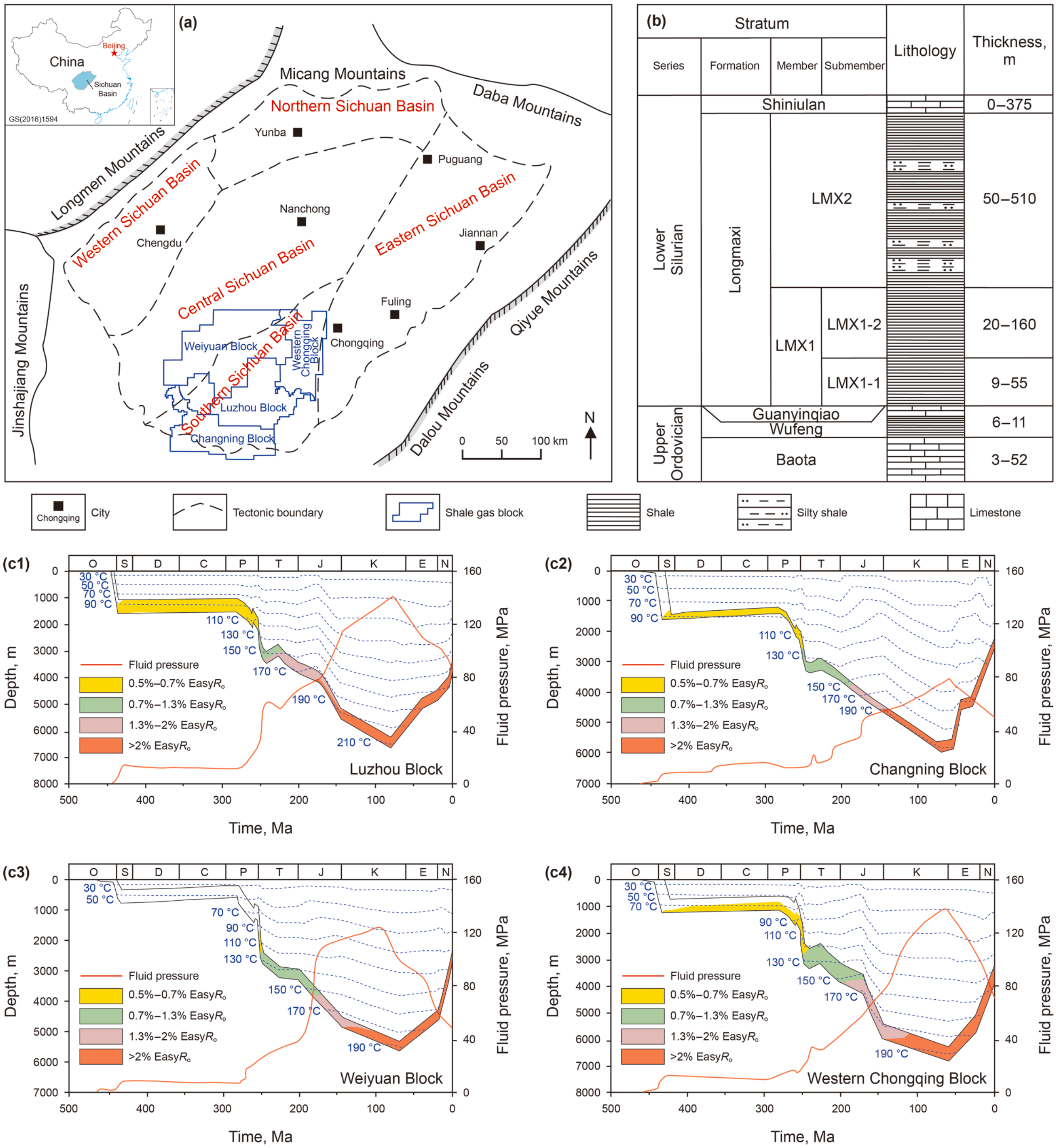

Fig. 1. Regional geological setting of the Wufeng–Longmaxi Formation in southern Sichuan Basin. **(a)** Structural framework of Sichuan Basin showing the four major study blocks in southern Sichuan Basin; **(b)** lithological columnar section of the sedimentary sequence; **(c1)–(c4)** burial history, thermal history, and formation fluid pressure evolution of the Luzhou, Changning, Weiyuan, and Western Chongqing blocks, respectively. Formation pressure evolution data are from Miao et al. (2023); Nie et al. (2021); Sun et al. (2024); Wu et al. (2022).

The Upper Ordovician Wufeng Formation–Lower Silurian Longmaxi Formation was deposited in a deep-water shelf setting and constitutes a typical marine shale succession (Fig. 1(b)). Owing to its wide distribution, large thickness, and high organic-matter abundance, it is the principal target for shale-gas exploration in southern Sichuan Basin (Chen et al., 2024; Jin et al., 2018; Mu et al., 2025; Zhang et al., 2025). Organic-rich shale is mainly developed in the lower Member 1 of the Longmaxi Formation (LMX1-1) (Guo et al., 2004; Ma et al., 2020; Mou et al., 2014; Wang et al., 2015a, 2015b; Zhang et al., 2022), which is dominated by calcareous siliceous shale and siliceous shale and serves as the main producing interval in this study area. Organic matter in this interval is dominated by Types I and II kerogen. TOC ranges from 0.48% to 10.15%, but is mainly concentrated between 2.0% and 5.0%. Organic maturity is generally higher than 2.0% R_o, indicating an over-mature stage dominated by dry-gas generation (Borjigin et al., 2017; Ma et al., 2023; Xiao et al., 2015; Yang et al., 2015; Zhang et al., 2021; Zhao et al., 2016). Core data show that the average TOC contents of the Wufeng–Longmaxi Formation are 3.29% in Luzhou, 2.88% in Changning, 3.21% in Weiyuan, and 3.16% in

Western Chongqing. The corresponding average clay-mineral contents are 21.17%, 31.90%, 36.40%, and 23.96%, respectively.

Burial history and formation pressure evolution (Fig. 1(c)) indicate that the stratigraphic evolution of the Wufeng–Longmaxi Formation in southern Sichuan can be divided into three stages: rapid compaction, compaction and hydrocarbon generation, and uplift.

(1) Rapid compaction stage: This stage begins with initial deposition and continues until organic matter approaches the hydrocarbon-generation threshold (R_o < 0.5%). The Weiyuan Block exited this stage at approximately 253 Ma, whereas the Luzhou, Changning, and Western Chongqing blocks exited it at approximately 435 Ma. Following deposition, the Luzhou, Changning, and Western Chongqing blocks underwent rapid subsidence, resulting in a rapid increase in burial depth. In contrast, the Weiyuan Block experienced only limited initial subsidence and underwent a minor uplift lasting approximately 150 Myr, after which subsidence resumed. By the end of this stage, burial depths were 1585 m (Luzhou), 1610 m (Changning), 1530 m (Weiyuan), and 1240 m (Western Chongqing). Formation pressures in all four blocks were hydrostatic, primarily controlled by overlying strata, with no abnormal pressures observed.

(2) Compaction and hydrocarbon generation stage: This stage is the key period of shale-reservoir evolution and spans approximately 253–69 Ma for Weiyuan, 435–80 Ma for Luzhou, 435–70 Ma for Changning, and 435–60 Ma for Western Chongqing. During this stage, organic matter entered the hydrocarbon-generation window (R_o = 0.5%), and maturity increased continuously to values above 2.5% in all four blocks. After entering this stage at approximately 253 Ma, the Weiyuan Block underwent progressive burial. In contrast, the Luzhou, Changning, and Western Chongqing blocks entered this stage at approximately 435 Ma, experienced a minor uplift lasting approximately 150 Myr, after which burial depth and organic maturity increased. These three blocks also underwent another brief uplift between approximately 245 Ma and 225 Ma, after which subsidence resumed. Changning maintained steady subsidence, while the other three blocks showed variable patterns (slow–fast–slow) until reaching maximum burial. Maximum burial depths and maturities (shallowest to deepest) were: Weiyuan (5620 m, R_o = 2.89%), Changning (5990 m, R_o = 2.85%), Luzhou (6590 m, R_o = 3.51%), and Western Chongqing (6730 m, R_o = 3.21%). Reservoir diagenesis during this stage was controlled by both inorganic (mechanical compaction) and organic (hydrocarbon generation) processes, with abnormal formation pressures developing due to hydrocarbon generation.

(3) Uplift stage: From the end of compaction and hydrocarbon generation to the present, this stage marks the cessation of hydrocarbon generation. Uplift in Changning occurred in four phases (slow–fast–slow–fast), with the largest magnitude and highest rate. Weiyuan and Western Chongqing experienced two phases (slow then fast), whereas Luzhou had the smallest uplift. Regarding formation pressure, Changning and Western Chongqing showed relatively steady reductions, while Luzhou and Weiyuan underwent multi-stage (fast–slow–fast) pressure declines. Present-day burial depths are 3780 m (Luzhou), 2600 m (Changning), 2780 m (Weiyuan), and 3920 m (Western Chongqing), with corresponding formation pressures of 86, 50, 47, and 70 MPa. These differences in uplift and pressure evolution provide critical insights into the late-stage modification and preservation of shale gas reservoirs.

3. Evolution model of shale porosity

3.1. Theoretical model

Shale pores can be classified into two main types based on reservoir space: inorganic pores and organic pores. The evolution of porosity over geological time can be summarized as follows:

$$\varphi(t) = \varphi_{\mathrm{inOM}}(t) + \varphi_{\mathrm{OM}}(t) \tag{1}$$

where $\varphi(t)$, $\varphi_{\mathrm{inOM}}(t)$, and $\varphi_{\mathrm{OM}}(t)$ denote the total, inorganic, and organic porosity, respectively, at a given geological time; all values are expressed in %.

Here, Eq. (1) is used as an operational decomposition of total porosity. We acknowledge that organic matter may locally occupy or line pre-existing inorganic pores, so the two pore systems are not necessarily perfectly exclusive; however, such overlap is treated as a secondary effect and is not parameterized explicitly in this study.

Following initial sediment deposition, burial compaction leads to particle rearrangement, gradually reducing overall inorganic porosity (Anovitz et al., 2013; Athy, 1930; Dewhurst et al., 1999; Emmanuel et al., 2015; Neuzil, 1994). Simultaneously, geochemical processes, such as mineral precipitation and dissolution, can substantially alter pore networks, either enlarging or reducing void spaces (Anovitz and Cole, 2015; Emmanuel et al., 2010; Navarre-Sitchler et al., 2009; Stack et al., 2014). Consequently, inorganic porosity in shale (φ_{inOM}) is primarily controlled by two main factors: (1) mechanical compaction and (2) mineral dissolution–precipitation reactions. This process can be written as:

$$\varphi_{\mathrm{inOM}}(t) = \varphi_{\mathrm{inOM}}(0) - \Delta\varphi_{\mathrm{mp}}(t) + \Delta\varphi_{\mathrm{dissolved}}(t) - \Delta\varphi_{\mathrm{precipitated}}(t) \tag{2}$$

where $\varphi_{\mathrm{inOM}}(0)$ is the initial inorganic porosity at deposition, %; $\Delta\varphi_{\mathrm{mp}}(t)$ is the porosity loss due to mechanical compaction, %; $\varphi_{\mathrm{dissolved}}(t)$ is the porosity increase from mineral dissolution, %; $\Delta\varphi_{\mathrm{precipitated}}(t)$ is the porosity reduction from mineral precipitation, %.

In principle, inorganic porosity may be influenced by both mechanical compaction and chemical diagenesis (dissolution/precipitation). For the studied LMX1-1, the present implementation does not explicitly parameterize mineral-specific chemical terms and instead treats the net chemical contribution as a second-order effect at the working scale of this study. Representative FE-SEM observations do not show pervasive pore-filling silica/quartz cement at the examined scale, although local silica redistribution cannot be ruled out. Therefore, the compaction-dominated model used here should be regarded as a first-order approximation rather than as evidence that quartz cementation is absent.

During hydrocarbon generation from organic matter, solid organic matter is transformed into liquid or gaseous hydrocarbons. This transformation induces volume changes in the original solid matter, leading to the formation of organic pores. The size of these organic pores is mainly determined by the type, abundance, and maturity of the organic matter. For a given type of organic matter, the evolution of its organic porosity over geological time can be described mathematically as:

$$\varphi_{\mathrm{OM}}(t) = f(\mathrm{TOC}, R_o) \tag{3}$$

After determining separately: (1) the initial porosity at the time of sediment deposition, (2) the effects of compaction, dissolution, and precipitation on inorganic pores, and (3) the quantitative evolution of organic porosity, a quantitative model for the evolution of total porosity over geological time can be established.

3.2. Actual porosity evolution model of the Wufeng–Longmaxi Formation in southern Sichuan Basin

3.2.1. Inorganic porosity evolution model

The change in porosity due to mineral precipitation and dissolution is governed by the rates and durations of these reactions (Appelo and Postma, 2004; Baqer and Chen, 2022; Hommel et al., 2018). Shale reservoirs in the Wufeng–Longmaxi Formation of southern Sichuan Basin display low porosity and poor permeability, resulting in limited fluid exchange. Consequently, the effects of dissolution and precipitation on porosity are relatively minor (Wang et al., 2012, 2014; Zou et al., 2010). Therefore, in this study, inorganic porosity evolution is modeled primarily as a function of burial-driven mechanical compaction. To quantitatively describe the effect of mechanical compaction on inorganic porosity, the exponential model proposed by Athy (1930) is widely used to describe the compaction process (Guo et al., 2017; Korvin, 1984; Puttiwongrak et al., 2020; Yang and Guo, 2020b).

$$\varphi_{\mathrm{inOM}} = \varphi_0 \times \mathrm{e}^{-cz} \tag{4}$$

where φ_{inOM} represents the inorganic porosity retained after burial compaction at depth z, %; φ_0 represents the initial porosity of the original sediment, %; c is a region-dependent compaction coefficient; and z denotes burial depth, km. The initial porosity of sediments is influenced by multiple factors, including variations in sediment composition and hydrodynamic conditions during deposition. Studies on subaqueous sediments, such as lake-floor and seabed deposits, indicate that initial porosity typically ranges from 50% to 70%. (Chen and Tian, 1989; Giles et al., 1998; Hegarty et al., 1988; Sclater and Christie, 1980; Underdown and Redfern, 2008; Zhang et al., 1992). The Athy model was originally developed for argillaceous sediments; here, its exponential form is used as a locally calibrated first-order approximation of burial-driven compaction. For the quartz-rich LMX1-1, the fitted coefficient c implicitly incorporates lithology-specific compaction behavior, including the relatively rigid quartz-clay framework.

In constructing a quantitative evolutionary model for inorganic porosity, accurately determining the inorganic porosity of shale reservoirs is the critical first step. Previous studies indicate that total organic carbon (TOC) exerts an important control on porosity development in the Wufeng–Longmaxi Formation shale reservoirs of southern Sichuan (Chen et al., 2012; Ma et al., 2020), although other factors such as mineral composition, formation pressure, and burial depth may also contribute.

In this study, inorganic porosity was quantified using the intercept of the porosity–TOC regression for well/interval datasets in which porosity shows a strong positive linear correlation with TOC. In such datasets, a distinct linear relationship exists between shale porosity and TOC (Fig. 2(a)), indicating that TOC is the dominant control on porosity variation; the intercept of this regression is taken as the inorganic porosity of the shale interval. Conversely, when no clear correlation exists between porosity and TOC (Fig. 2(b)), TOC cannot be considered the dominant control, and the intercept method is not regarded as applicable.

To ensure transparency and reproducibility, objective screening criteria were applied to each well/interval dataset: $n \geq 10$, positive slope ($k > 0$), $R^2 \geq 0.70$, and a statistically significant slope

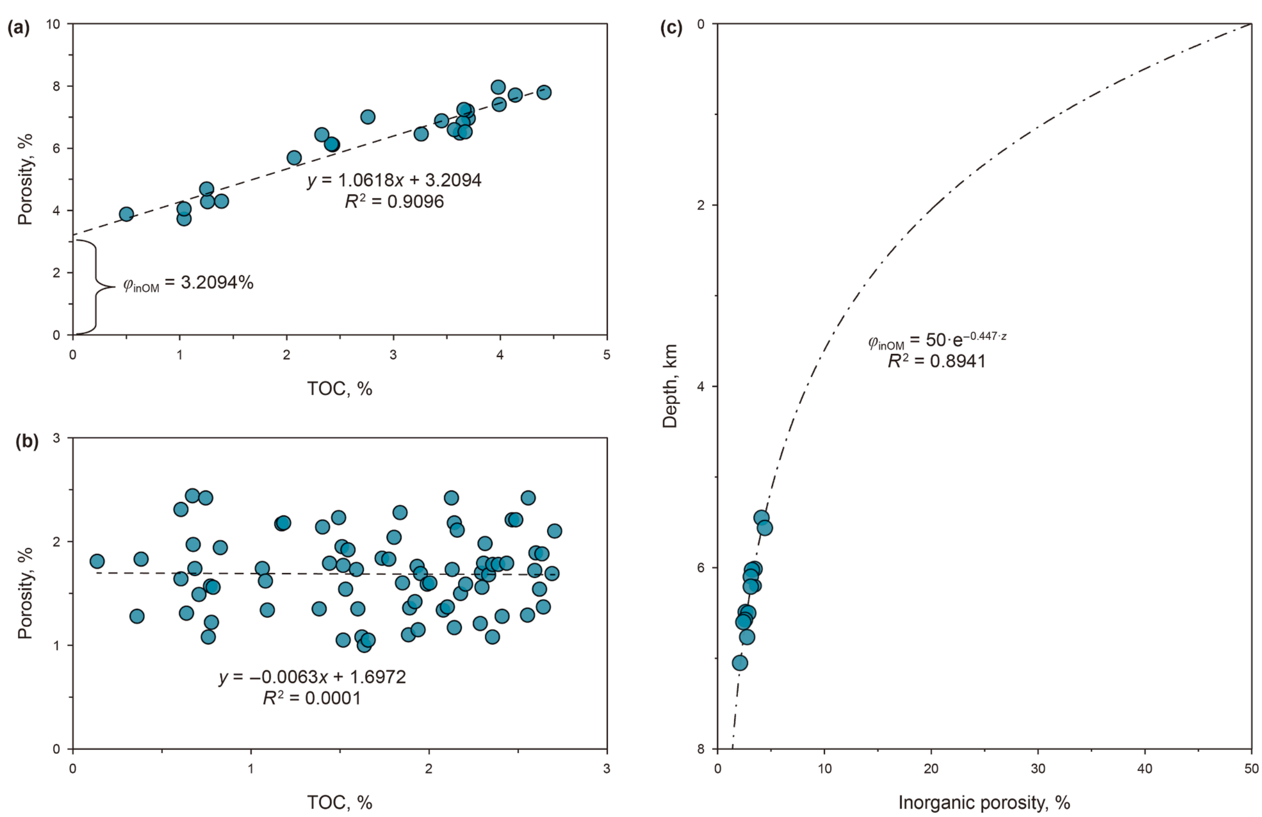

Fig. 2. Methodology for determining inorganic porosity and its evolutionary model. **(a)** Strong linear positive correlation between porosity and TOC, where inorganic porosity equals the intercept value; **(b)** no significant linear relationship between porosity and TOC; inorganic porosity cannot be derived through this method; **(c)** evolutionary model of inorganic porosity.

($p < 0.01$). A total of 36 well/interval datasets with paired porosity–TOC measurements were initially screened, of which 13 wells (total $n = 368$ data points) satisfied these criteria, with $n = 14$–56 per well and $R^2 = 0.735$–0.910; the remaining 23 datasets were rejected because they failed one or more screening conditions. These rejected datasets were not discarded arbitrarily; rather, they represent intervals in which TOC is not the dominant control on porosity, and therefore the intercept method is not considered applicable. Regression statistics and intercept uncertainty (95% confidence interval) for the accepted datasets are provided in Supplementary Table S1.

By applying Eq. (4) to the inorganic porosity data from multiple shale gas wells, an evolutionary model for inorganic porosity in the Wufeng–Longmaxi Formation shale gas reservoirs of southern Sichuan Basin was established (Fig. 2(c)).

$$\varphi_{\mathrm{inOM}} = 50 \cdot \mathrm{e}^{-0.447 \cdot z} \tag{5}$$

3.2.2. Organic porosity evolution model

Benefiting from advances in electron microscopy, the combined technique of argon-ion polishing and scanning electron microscopy (SEM) can now clearly resolve widely developed micro- to nanoscale organic pores in shale reservoirs (Lin et al., 2024; Loucks et al., 2012; Wu et al., 2015). In this study, organic matter surface porosity was quantitatively extracted from argon-ion polished field emission scanning electron microscopy (FE-SEM) images of shale samples at varying maturities using ImageJ software. The methodology is detailed as follows.

(1) Acquire nanoscale-resolution micrographs in backscattered electron (BSE) mode using FE-SEM. Select organic matter regions for zoomed-in observation and image acquisition (Fig. 3(a)).

(2) Apply gray-scale threshold extraction in ImageJ to isolate organic matter (Fig. 3(b)) and pore areas within organic matter (Fig. 3(c)).
(3) Calculate organic matter surface porosity using Eq. (6).

$$P_{\mathrm{S}} = \frac{S_{\varphi\text{-OM}}}{S_{\mathrm{OM}}} \times 100\% \tag{6}$$

where P_{S} is the organic-matter surface porosity, %; $S_{\varphi\text{-OM}}$ is the organic matter pore area, nm^2; S_{OM} is the organic matter area, nm^2.

High-resolution SEM images effectively mitigate the challenge of accurately identifying organic micropores. However, due to the limited field of view, results from a single SEM image cannot fully represent the actual conditions of the sample. Therefore, the average organic matter surface porosity from 20 SEM images was used to characterize the sample's porosity. For each sample, 20 non-overlapping FE-SEM images were acquired from organic-matter-bearing regions distributed across the polished surface. The images used for P_{S} extraction typically had pixel sizes on the order of 4–10 nm and field-of-view widths of approximately 2–10 μm, depending on the image used. Image locations were selected to represent different organic-matter patches within the sample, rather than being concentrated on a single pore-rich domain. Accordingly, P_{S} in this study is defined as the surface porosity within organic-matter domains, not as a whole-rock areal porosity.

Because the Wufeng–Longmaxi Formation in southern Sichuan generally corresponds to the high- to post-maturity stage, published P_{S} data from other Type I–II kerogen-bearing shale formations were incorporated to extend the maturity coverage of the dataset. These external datasets were used to constrain the generalized empirical shape of the P_{S}–R_{o} relationship, rather than to imply that organic-porosity evolution is strictly formation-independent. Accordingly, the fitted curve in Fig. 4 should be regarded as a first-order maturity-dependent empirical trend for Types I–II organic-rich shales. The compiled dataset suggests that P_{S} first increases and then decreases with maturity, displaying an overall parabolic trend (Fig. 4). At increasing maturity, organic pores are generated as kerogen/bitumen transforms and hydrocarbons are expelled, whereas at very high maturity the organic pore system may partially collapse/shrink under sustained high effective stress and structural reorganization of organic matter (e.g., aromatization/graphitization), and/or be occluded by pyrobitumen and minor diagenetic infilling, leading to an apparent porosity decrease (Cao et al., 2021; Hou et al., 2019; Yang et al., 2022, 2025).

Based on the correlation between organic matter surface porosity and total organic porosity, surface porosity was converted to total organic porosity using Eq. (7) (Chen and Jiang, 2016; Jarvie et al., 2007):

$$\varphi_{\mathrm{OM}} = \frac{P_{\mathrm{S}}}{100} \cdot \mathrm{TOC} \cdot \frac{\rho_{\mathrm{rock}}}{\rho_{\mathrm{OM}}} \cdot \gamma \tag{7}$$

where ρ_{rock} is the shale density (≈2.7 g/cm^3); ρ_{OM} is the density of organic matter in shale (≈1.2 g/cm^3); TOC is the total organic carbon, %; and γ is the conversion coefficient between organic matter content and TOC content. A central value of $\gamma = 1.2$ is adopted for point estimates, whereas its uncertainty is propagated in Section 3.2.4.

By converting the organic matter surface porosity at varying maturity levels to organic porosity, the evolutionary model of organic porosity can be established:

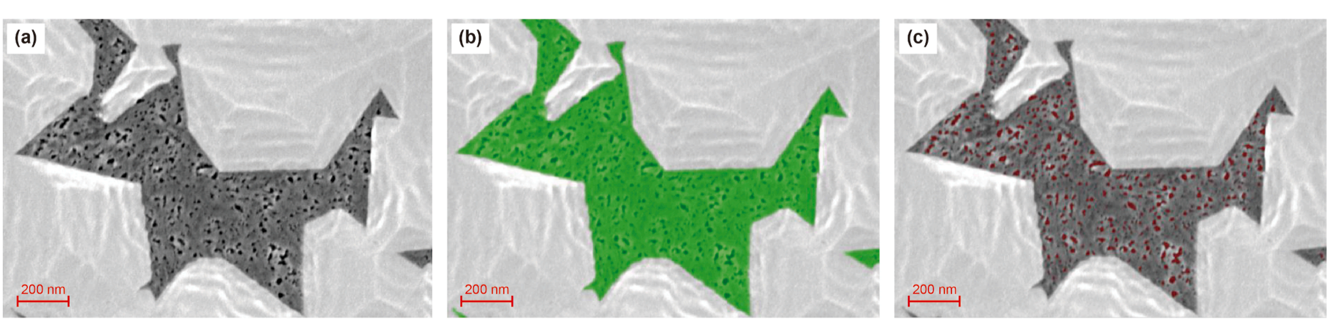

Fig. 3. Methodology for identifying organic matter surface porosity. **(a)** Original scanning electron microscopy (SEM) image, **(b)** extracted organic matter area, **(c)** extracted organic matter pore area.

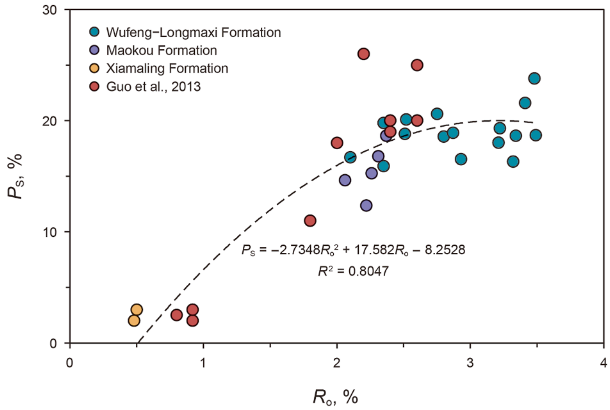

Fig. 4. Generalized maturity-dependent empirical trend of organic-matter surface porosity (P_S). The plotted data points are shown directly in the figure and were compiled from the Wufeng–Longmaxi Formation in this study and published Type I–II organic-rich shale data from previous studies (Guo et al., 2013, 2017; Yu and Tang, 2019). The fitted curve represents a first-order empirical trend rather than a formation-independent universal relationship. For $R_o < 0.5\%$, P_S is treated as negligible in practical application.

$$\varphi_{OM} = \frac{\left(-2.7348{R_o}^2 + 17.582R_o - 8.2528\right)}{100} \cdot TOC \cdot 2.7 \tag{8}$$

For practical application, the fitted P_S–R_o relation is used only within the maturity range represented by the compiled dataset. Because organic pores are negligible before the onset of hydrocarbon generation, P_S is taken as approximately zero for $R_o < 0.5\%$.

3.2.3. Pressure-confined porosity correction

Under the influence of effective stress, reservoir porosity under subsurface high-pressure conditions typically differs from laboratory-measured core porosity at ambient pressure. To obtain accurate porosity values under subsurface high-pressure conditions, pressure-confined porosity experiments were conducted to calibrate the correction model (Blach et al., 2021; Huang and Wang, 2007; Wang et al., 2017; Zhang and Yue, 2021).

The pressure-confined porosity experiments were performed using the PoroPDP-200 pressure-confined porosity-permeability measurement system at Northeast Petroleum University. All test samples were collected from the LMX1-1 of the Wufeng–Longmaxi Formation in the southern Sichuan Basin (Table 1). Additionally, TOC and whole-rock XRD analyses were conducted to investigate the factors influencing pressure-confined porosity (Table 1).

The experimental results demonstrate that porosity decreases significantly with increasing effective stress, and this variation can be effectively characterized by a power function (Eq. (9)) (Fig. 5).

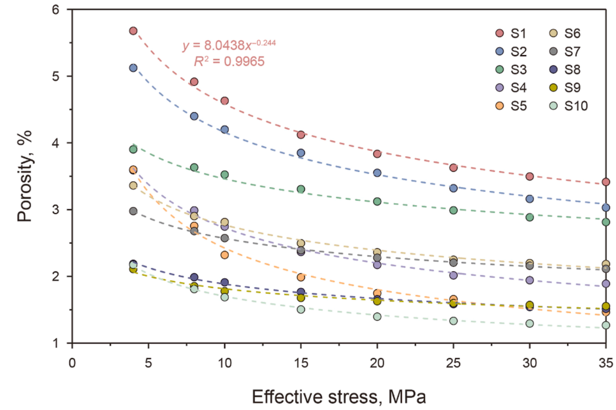

Fig. 5. Porosity–effective-stress curves of the ten shale samples used for pressure-confined porosity calibration.

$$\varphi_\sigma = \alpha \cdot \sigma^{-\beta} \tag{9}$$

where φ_σ is the porosity under subsurface high-pressure conditions at varying effective stresses, %, hereafter uniformly referred to as in situ porosity; σ is the effective stress, MPa; α and β are fitting parameters.

The pressure-confined porosity experiments were conducted over an effective-stress range of $\sigma = 4$–35 MPa (Fig. 5), which defines the calibration range of Eq. (10). In the burial-history reconstruction, effective stress is calculated as $\sigma = \sigma_V - P_P$, where σ_V is the overburden stress estimated from burial depth and P_P is the formation pressure constrained by the pressure-evolution history shown in Fig. 1(c). Under maximum-burial conditions, σ may reach approximately 105 MPa in the deepest blocks; therefore, using Eq. (10) for $\sigma > 35$ MPa is an explicit extrapolation and should be interpreted as a first-order estimate with increased uncertainty. The calibration results indicate that parameter α exhibits a linear positive correlation with conventional porosity (Fig. 6(a)). Parameter β shows systematic relationships with TOC (Fig. 6(b)) and mineral composition, especially clay and quartz contents (Fig. 6(c)). Furthermore, β is positively correlated with the TOC-to-clay mineral ratio (Fig. 6(d)). Therefore, β can be expressed as a function of TOC and clay mineral content. In summary, based on the analysis of pressure-confined porosity experimental data, a porosity correction model for Wufeng–Longmaxi Formation shale samples in southern Sichuan Basin was established as follows:

$$\varphi_\sigma = (1.4264\varphi - 1.1058) \cdot \sigma^{-\left(0.544\frac{TOC}{m_{clay}} + 0.1007\right)} \tag{10}$$

Because Eq. (10) is calibrated using a limited dataset ($n = 10$; Table 1), we explicitly report regression uncertainty and stability.

Table 1
Characteristics of pressure-confined porosity test samples.

Sample	TOC, %	Porosity, %	Mineral composition, %					
			Quartz	Clay	Feldspar	Calcite	Dolomite	Pyrite
S1	8.59	6.280	51.3	24.7	8	7	4.7	4.3
S2	5.75	5.866	57.1	23.3	5.5	3.8	8.1	2.2
S3	4.97	4.682	68.2	13.1	2.9	4.2	8.9	2.7
S4	10.15	4.836	39.6	19.2	15.1	10.3	9.8	6.0
S5	1.97	2.544	45.6	17.4	18	7.8	8.9	2.3
S6	4.20	4.486	44.1	28	5.8	13.1	3.8	5.2
S7	6.90	4.244	35.2	35.7	8.3	5.5	5.0	10.3
S8	3.37	3.660	54.4	23.5	5.7	4.5	8.1	3.8
S9	2.76	2.633	59.3	25.5	4.7	2.3	3.2	5.0
S10	1.55	2.653	56.2	9.3	9.8	9.1	10.4	5.2

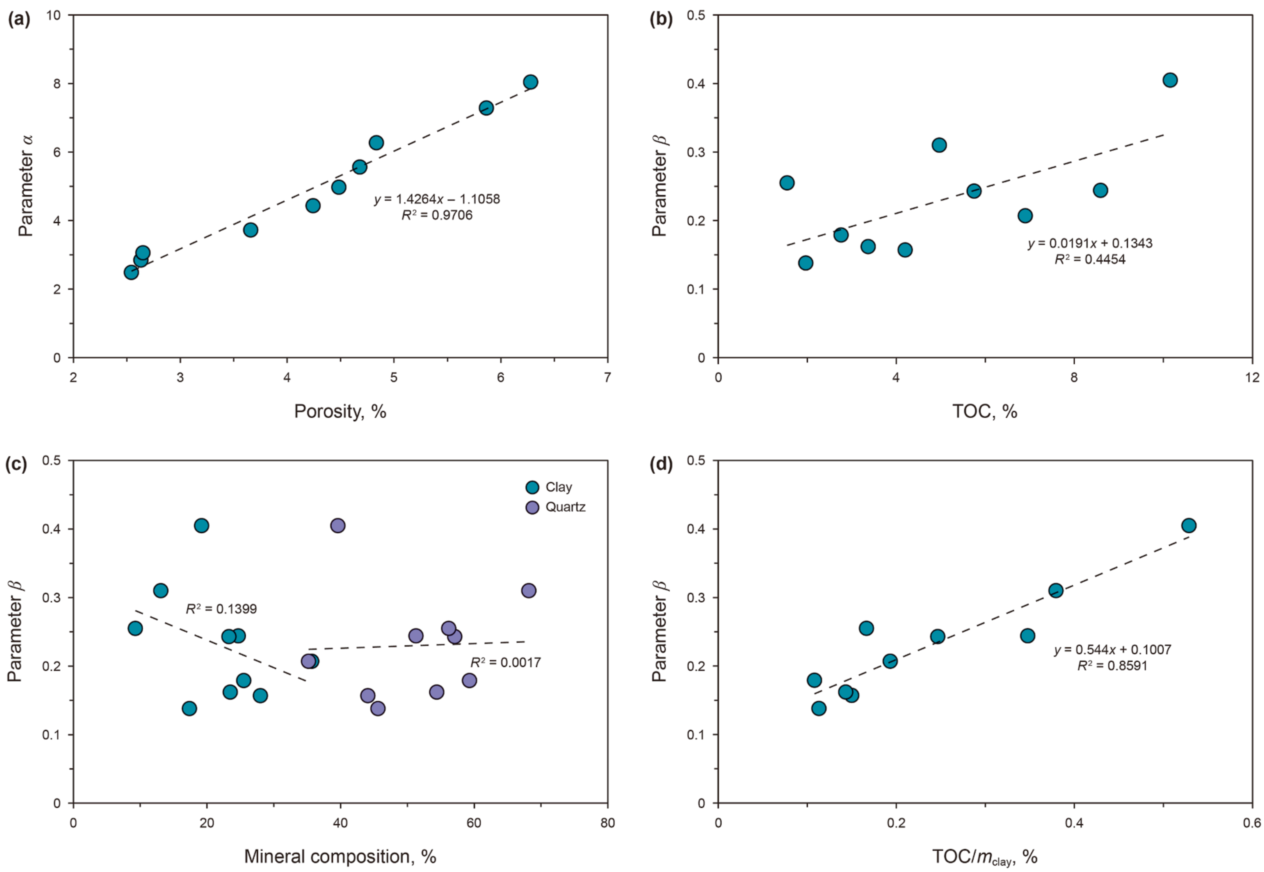

Fig. 6. Relationships between parameters of the pressure-confined porosity model and reservoir characteristics. **(a)** Relationship between conventional porosity and parameter α, **(b)** relationship between parameter β and TOC, **(c)** relationships between parameter β and clay and quartz contents, **(d)** relationship between parameter β and the ratio of TOC to clay mineral content (TOC/m_{clay}).

Coefficient uncertainty is evaluated using non-parametric bootstrap resampling (5000 resamples), and predictive stability is assessed using leave-one-out cross-validation; results are summarized in Supplementary Table S2. The recommended application domain in terms of sample properties is restricted to the calibration ranges (TOC = 1.55%–10.15%; φ = 2.544%–6.28%; m_{clay} = 9.3%–35.7%). In the burial-history application, σ may reach ~105 MPa, exceeding the experimental σ range (4–35 MPa); therefore, predictions at σ > 35 MPa are extrapolated and are interpreted with increased uncertainty, which is propagated from the regression uncertainty reported in Supplementary Table S2.

3.2.4. Uncertainty assessment and reporting

Uncertainty arises from five main steps in the workflow: (1) intercept estimation from porosity–TOC regressions, (2) compaction-model fitting, (3) SEM/ImageJ-based P_S extraction and conversion to organic porosity, (4) effective-stress correction using Eqs. (9) and (10), and (5) burial/pressure reconstruction used to calculate σ through time. For regression-based components, parameter uncertainty is quantified by non-parametric bootstrap resampling and reported as 95% confidence intervals (Supplementary Table S1 for intercept-derived inorganic porosity; Supplementary Table S2 for the stress-correction regressions). For Monte Carlo propagation, the intercept-derived inorganic-porosity uncertainty was approximated as SD_inorg = 0.20 porosity percentage points based on Supplementary Table S1.

For P_S, more than half of the compiled data are taken from published studies lacking replicate-image statistics. The replicate SEM/ImageJ results from a representative sample analyzed in this study (n = 20 images; mean (P_S) = 18.65%, SD (P_S) = 2.82%, CV ≈ 15%) are therefore used only to characterize within-sample image variability, whereas an additional broader uncertainty term corresponding to CV = 25% is assigned in the Monte Carlo analysis to account for between-sample and inter-study variability in literature-derived P_S values.

The Monte Carlo propagation also treats γ in Eq. (7) as uncertain, using γ = 1.2 as the central value and sampling over 1.10–1.35. In addition, because α in Eq. (10) is estimated from conventional porosity (Fig. 6(a)), laboratory porosity uncertainty is propagated through the correction chain and approximated as Uniform (−0.2, +0.2) porosity units based on instrument repeatability.

All uncertainties are propagated to key outputs by Monte Carlo sampling, and the results are reported as point estimates, medians, and 95% prediction intervals (PI) in Supplementary Table S3.

4. Organic–inorganic porosity evolution of Wufeng–Longmaxi shale gas reservoirs

Based on the burial and thermal histories of the Luzhou, Changning, Weiyuan, and Western Chongqing blocks in the southern Sichuan Basin, a quantitative model of coupled organic–inorganic porosity evolution was established. Using burial and thermal histories together with the inorganic- and organic-porosity models, total porosity was reconstructed, and pressure-confined porosity experiments were used to restore in situ porosity (Fig. 7). The evolutionary features are summarized as

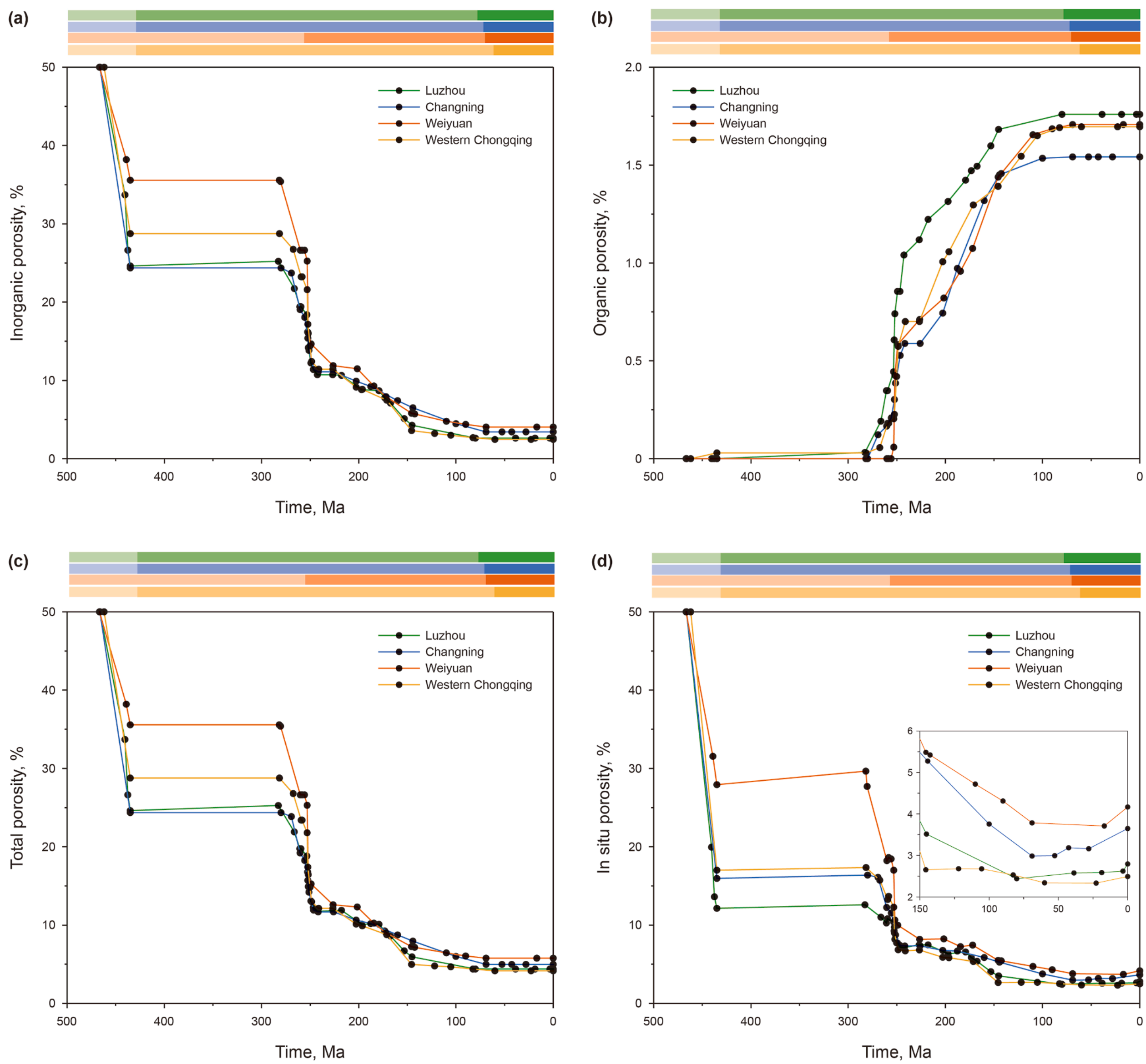

Fig. 7. Porosity evolution through geological time in four shale-gas blocks and the three-stage evolution framework. **(a)** Inorganic porosity, **(b)** organic porosity, **(c)** total porosity, **(d)** in situ porosity versus time (Ma). Curves denote the Luzhou, Changning, Weiyuan, and Western Chongqing blocks, respectively. The three evolutionary phases discussed in the text are annotated by the colored ribbons at the top of each panel for each block (same hue as the corresponding curve): light, medium, and dark shades indicate Stage (1) (rapid compaction), Stage (2) (compaction coupled with hydrocarbon generation), and Stage (3) (tectonic uplift/unloading).

follows (all block-specific porosity values reported below are point estimates; the associated uncertainty bounds, including medians and 95% prediction intervals, are summarized in Supplementary Table S3).

(1) Rapid compaction stage:

Organic pores had not yet developed, and total porosity was therefore identical to inorganic porosity. Inorganic porosity decreased rapidly with increasing burial depth (initially ~50%), dropping to ~25% in the Luzhou, Changning, and Weiyuan blocks and to ~28% in the Western Chongqing block, indicating strong mechanical compaction under increasing effective stress. After pressure-confined porosity correction, in situ porosity declined markedly to 12.13% (Luzhou), 15.97% (Changning), 17.00% (Weiyuan), and 17.02% (Western Chongqing), consistent with effective-stress-controlled closure of compaction-sensitive inorganic pores. Minor deviations (e.g., a slight rebound in Weiyuan) correspond to short-term tectonic adjustments, but the first-order trend is compaction-dominated.

(2) Compaction and hydrocarbon generation stage:

Organic matter entered the hydrocarbon generation window and organic pores gradually formed. The Luzhou, Changning, and Western Chongqing blocks entered the hydrocarbon-generation window earlier than the Weiyuan block, because they experienced earlier deep burial, whereas the Weiyuan Block reached the threshold later owing to its slower initial subsidence and delayed burial. However, the Luzhou, Changning, and Western Chongqing blocks underwent an early regional uplift lasting approximately 150 Myr, which interrupted continuous subsidence; consequently, organic porosity increased only slightly during the early part of this phase. In contrast, the Weiyuan Block reached the hydrocarbon-generation threshold after this uplift episode and therefore did not show the same early gradual increase. Following renewed subsidence, organic pores developed rapidly in all four blocks. The maximum reconstructed organic porosity along the burial path reached 1.79% in Luzhou, 1.54% in Changning, 1.71% in Weiyuan, and 1.70% in Western Chongqing. For the Luzhou block, the organic porosity at final maximum burial was 1.76%, only slightly lower than the path maximum of 1.79%. This very small difference indicates that the peak organic-porosity development in Luzhou occurred very close to the maximum-burial stage. Although Luzhou reached the highest maturity at maximum burial (R_o = 3.51%), the generalized P_S–R_o trend in Fig. 4 suggests that organic-pore development may peak near the turning point of the curve and then weaken only slightly at the highest over-mature stage. Meanwhile, inorganic porosity continued to decline with burial depth and reached minima of 2.63% (Luzhou), 3.43% (Changning), 4.05% (Weiyuan), and 2.47% (Western Chongqing) at maximum burial. Because the rate of organic-pore creation was slower than the compaction-driven loss of inorganic porosity, total porosity decreased continuously; the final total porosity at maximum burial is 4.39% (median 4.42%, 95% PI: 3.84%–5.00%) for Luzhou, 4.98% (median 5.00%, 95% PI: 4.55%–5.48%) for Changning, 5.76% (median 5.81%, 95% PI: 5.31%–6.28%) for Weiyuan, and 4.16% (median 4.19%, 95% PI: 3.71%–4.71%) for Western Chongqing. These trajectories indicate that mechanical compaction remains the dominant control on total-porosity evolution, whereas organic porosity provides a secondary contribution once hydrocarbon generation starts.

After pressure-confined porosity correction, in situ porosity generally decreased, but distinct fluctuations occurred when rapid hydrocarbon generation (R_o increasing from ~1% to ~2%) coincided with the development of abnormal formation pressure. Such pressure build-up temporarily reduced effective stress and produced staged increases in the Luzhou and Weiyuan blocks (250–150 Ma), and a similar pattern in the Western Chongqing Block (120–105 Ma), even though inorganic porosity continued to decline. With progressive burial, in situ porosity ultimately stabilized at low values of 2.44% (Luzhou), 2.98% (Changning), 3.78% (Weiyuan), and 2.34% (Western Chongqing).

(3) Uplift stage:

During the uplift stage, thermal maturity ceased to increase, and inorganic, organic, and total porosity remained nearly constant. By contrast, in situ porosity evolved in a block-dependent manner, reflecting the competition between overburden unloading and formation-pressure dissipation, i.e., the effective-stress trajectory. The Luzhou Block shows a modest rebound from 2.44% at ~80 Ma to 2.79% at present, indicating that unloading only slightly exceeded pressure loss. The Changning Block exhibits the strongest rebound and the most pronounced fluctuations, ultimately reaching 3.65%, consistent with a large uplift amplitude combined with relatively limited pressure dissipation. In the Weiyuan block, in situ porosity decreases slightly during early uplift and then rebounds rapidly to 4.17%, suggesting an initial stage of faster pressure decline followed by accelerated uplift/unloading. By contrast, the Western Chongqing Block shows only a minor rebound from 2.34% to 2.49%, implying faster pressure dissipation and/or weaker unloading effects. At present day, the restored in situ porosity is 2.79% for Luzhou (median 2.79%, 95% PI: 1.97%–3.85%), 3.65% for Changning (median 3.63%, 95% PI: 2.64%–4.92%), 4.17% for Weiyuan (median 4.16%, 95% PI: 3.02%–5.68%), and 2.49% for Western Chongqing (median 2.48%, 95% PI: 1.70%–3.55%).

Although the 95% prediction intervals of present-day in situ porosity are relatively broad and partly overlap, the point estimates and medians preserve the same first-order ranking, indicating that inter-block differences remain interpretable at the trend level. Consistent with this pattern, the overall differential evolution among blocks can be summarized as follows: (1) at maximum burial, inorganic porosity (and thus total porosity) is negatively correlated with burial depth and follows the same ranking, i.e., Weiyuan > Changning > Luzhou > Western Chongqing; (2) organic porosity primarily tracks TOC and varies within a narrow range because the four blocks share a relatively close maturity interval ($R_o \approx$ 2.5%–3.5%), with limited incremental maturity effects beyond $R_o \approx 2.5\%$ (Fig. 4); and (3) the late-stage rebound of in situ porosity is controlled by uplift magnitude/rate and the preservation or dissipation of abnormal pressure.

5. Discussion

5.1. Multi-scale conceptual model and synthesis of inter-block differences

The reconstructed porosity histories of the four blocks show a consistent three-stage framework but distinct block-level differences (Fig. 7). To generalize these differential behaviors, we present a comprehensive conceptual, multi-scale model (Fig. 8). At the pore scale, inorganic porosity is primarily reduced by mechanical compaction and stress-sensitive pore closure, whereas organic porosity is generated during thermal maturation and hydrocarbon generation. At the core/laboratory scale, FE-SEM/ImageJ quantifies organic-matter surface porosity and pressure-confined experiments constrain the effective-stress dependence of porosity. At the basin/structural scale, burial depth and the effective-stress trajectory (controlled by subsidence/uplift and abnormal-pressure generation and dissipation) determine the timing and magnitude of porosity loss, preservation, and rebound. Differences among blocks can therefore be understood as different combinations of (1) maximum burial depth, (2) pressure preservation versus dissipation, and (3) uplift magnitude and rate, superimposed on broadly similar maturity ranges.

Although chemical diagenesis (dissolution/precipitation) is included in the conceptual framework (Fig. 8), our quantitative implementation treats the net chemical modification of inorganic pore volume as a second-order term for the targeted LMX1-1. This simplification is intended for compaction-dominated, relatively closed-system marine shales in which pervasive cementation/dissolution is not evident at the studied scale. We therefore emphasize that the framework may require explicit chemical terms when applied to intervals characterized by strong fluid-rock interaction, extensive carbonate/silica cementation, or dissolution-driven secondary porosity.

(1) Effective-stress history (burial depth × overpressure preservation) as the first-order control. Mechanical compaction continuously reduces inorganic porosity during subsidence, and the magnitude of this reduction scales with maximum burial depth. Overpressure generated during intense hydrocarbon generation can partly counteract increasing overburden stress by lowering effective stress, producing staged in situ porosity fluctuations (Fig. 7(d)). In the study area, effective stress remained above ~30 MPa during most geological periods, even under elevated abnormal pressure, which explains the overall limited amplitude of within-block porosity variation.

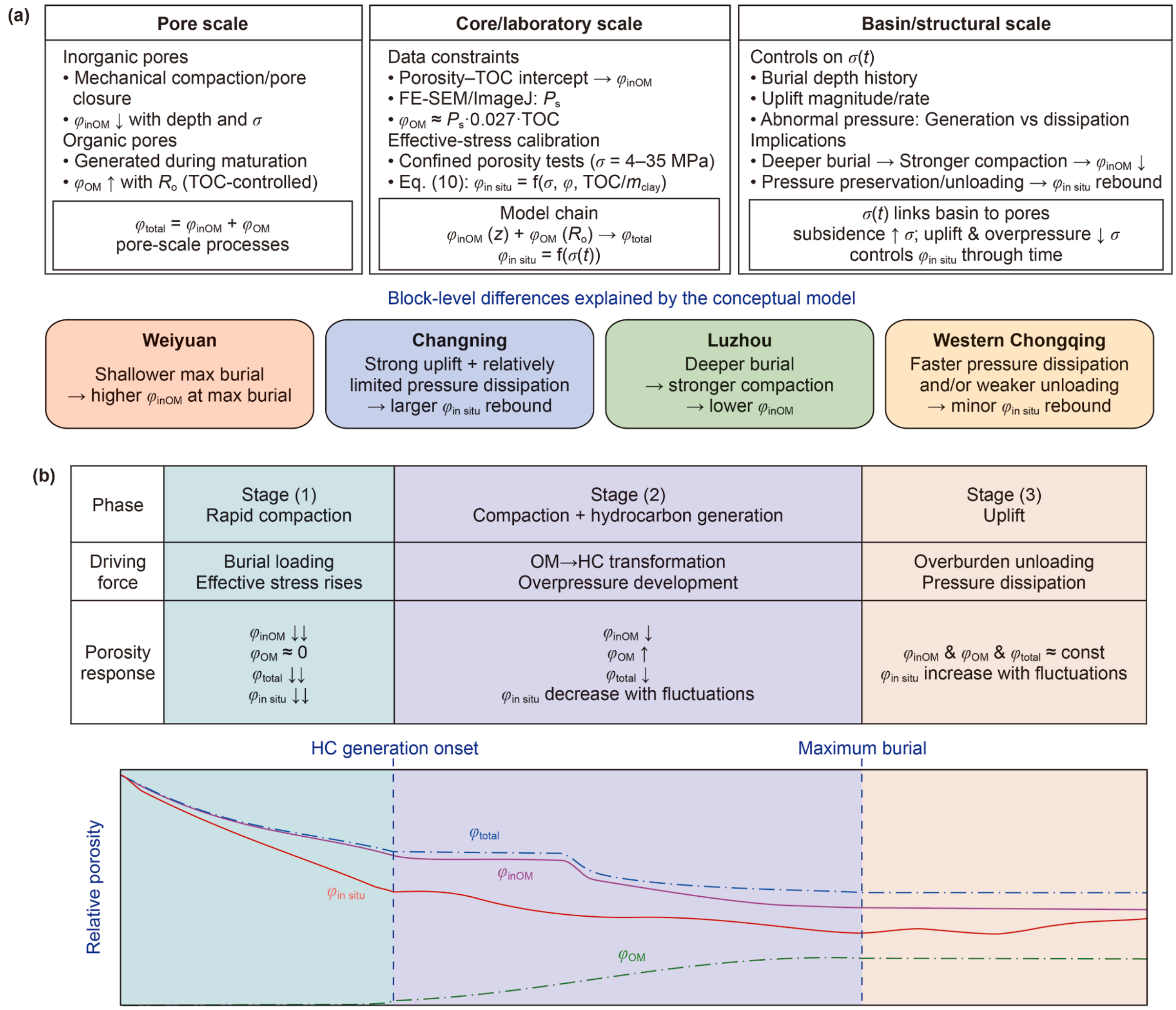

Fig. 8. Conceptual model for differential porosity evolution of the Wufeng–Longmaxi shales in southern Sichuan Basin. **(a)** Multi-scale framework showing the coupled controls of pore-scale processes, rock properties, and burial-pressure evolution on porosity development; **(b)** phase-based schematic illustrating the three-stage evolution of inorganic, organic, total, and in situ porosity.

(2) Organic matter abundance and the onset of hydrocarbon generation as the primary trigger for organic-pore development. Organic porosity initiates when maturity enters the hydrocarbon generation window and increases rapidly during strong hydrocarbon generation. However, for the maturity range of most blocks ($R_o \approx 2.5\%$–3.5%), organic-porosity growth becomes less sensitive to additional R_o increase, making TOC the dominant control on inter-block differences. At very high maturity ($R_o >$ ~3.5%), organic porosity may decrease due to pore shrinkage/collapse and/or occlusion, which reconciles the observation that the most mature block does not necessarily have the highest organic porosity.

(3) Mineral composition, framework/fabric, and compaction resistance at the core scale. Clay mineral content influences the initial inorganic pore inventory through clay interlayer pores, whereas the quartz-clay framework and fabric control compaction sensitivity. A more rigid framework can slow compaction-driven pore loss, while lower clay content decreases the clay-related inorganic pore contribution and can increase the relative proportion of organic pores.

(4) Uplift timing/rate and pressure dissipation as the trigger for late-stage in situ porosity rebound. Uplift reduces overburden stress and can increase restored in situ porosity, but the net rebound depends on whether formation pressure is preserved or dissipates rapidly. Blocks characterized by larger uplift amplitude/rate and relatively limited pressure dissipation (e.g., Changning) exhibit stronger rebound, whereas rapid pressure dissipation limits rebound even under comparable uplift magnitude (e.g., Western Chongqing).

From a reservoir-quality perspective, blocks characterized by shallower maximum burial and relatively limited pressure dissipation are more favorable for preserving inorganic pores and enhancing the late-stage rebound of in situ porosity. Therefore, integrating burial depth, pressure-preservation indicators, and TOC provides a practical basis for predicting high-quality shale reservoirs within over-mature marine systems.

Overall, the observed inter-block divergence can be captured by the proposed multi-scale framework: total-porosity differences are dominated by compaction-controlled inorganic porosity governed by effective-stress history, while organic porosity provides a secondary TOC-controlled contribution after the hydrocarbon-generation trigger. This interpretation provides a predictive basis for assessing reservoir quality and porosity preservation in deep to over-mature marine shales.

5.2. Comparison with previous studies and implications for reservoir quality

The reconstructed porosity evolution of the four key blocks in southern Sichuan indicates that final total porosity ranges from 4.16% to 5.76%, with an average of 4.82%, whereas organic porosity accounts for 29.63%–40.74%, with an average of 35.37% (Table 2). Compared with previous studies, the total porosity reported here is lower, whereas the proportion of organic porosity is higher. In addition to the exclusion of dissolution pores, the relatively low clay mineral content in the samples may explain this discrepancy. The samples analyzed in this study, taken from the LMX1-1, generally contain less clay than the overall Wufeng–Longmaxi Formation. Clay interlayer pores represent an important component of the inorganic pore system, and their reduction decreases total porosity while increasing the proportion of organic pores. For example, Guo et al. (2013) showed that when clay content is <40%, total porosity declines significantly while the proportion of organic pores increases. Similarly, Wang et al. (2014) reported that as clay content decreased from 46%–62% to 8%–29.1%, total porosity dropped from 6.4%–8.2% to 3.4%–5.7%, whereas organic porosity rose from 10%–17.7% to 20%–35.6%.

The inter-block divergence observed in this study indicates that final total porosity is dominated by the inorganic component, because compaction-driven inorganic pore loss scales with maximum burial depth, whereas differences in organic porosity are relatively small. Organic porosity among the four blocks is mainly controlled by TOC, but varies within a narrow range because all blocks fall within a similar over-mature interval ($R_o \approx 2.5\%$–3.5%). Consistent with the organic-porosity evolution model (Fig. 4), once R_o reaches about 2.5%, further maturity increase has only a limited incremental effect on organic pore development, and organic porosity may decrease slightly at the highest over-mature stage. This is particularly evident in the Luzhou block, where the maximum reconstructed organic porosity along the burial path is 1.79%, whereas the value at final maximum burial is 1.76%, indicating only a negligible reduction at the highest maturity. Therefore, the final total porosity largely mirrors the inorganic-porosity ranking, while the block-dependent rebound of in situ porosity during uplift reflects differences in uplift amplitude/rate and abnormal-pressure preservation. It should also be noted that part of the discrepancy between this study and previous studies may reflect methodological differences, because the present study and the previous studies summarized in Table 2 used different analytical workflows to partition inorganic and organic porosity.

Table 2
Comparison of porosity characteristics.

Source of data	Well or Area	TOC, %	Total porosity, %	Organic porosity percentage, %
This study	Luzhou Block (Well D201)	3.29	4.39	40.11
	Changning Block (Well N201)	2.88	4.98	30.98
	Weiyuan Block (Well W202)	3.21	5.76	29.63
	Western Chongqing Block (Well Z202)	3.16	4.16	40.74
	Average	3.14	4.82	35.37
Wang et al. (2014)	Well CX 1	4.0	5.4	24.9
Wang et al. (2015b)	Well JY 1	2.6	4.6	23.91
	Well JY 4	2.9	4.6	28.26
Guo et al. (2013)	Sichuan Basin	3.3	5.3	24.6
	Well CX1 & Well N201	3.3	5.88	34.2
	Well W201	2.7	5.46	12.8

5.3. Limitations of evolutionary models

Despite the development of a porosity evolution model, several limitations remain.

(1) Chemical diagenesis of inorganic pores (applicability boundary). Our conceptual framework acknowledges that inorganic porosity may be modified by mineral dissolution and precipitation. However, these chemical terms were not explicitly parameterized in the quantitative reconstruction for the LMX1-1. This is because the Wufeng–Longmaxi depositional system is generally considered relatively closed, with limited large-scale fluid exchange, and the studied interval contains relatively little clay, reducing the likelihood that clay-related chemical transformation dominates the inorganic pore budget. Accordingly, the present implementation focuses on compaction-driven pore loss and treats the net chemical contribution ($\Delta\varphi_{\text{chem}} = \Delta\varphi_{\text{dissolved}} - \varphi_{\text{precipitated}}$) as a second-order effect. Representative FE-SEM observations from the studied interval do not show pervasive pore-filling silica/quartz cement at the examined scale, although local silica redistribution cannot be ruled out.

Using the inorganic porosity at maximum burial obtained in this study (Weiyuan 4.05%, Changning 3.43%, Luzhou 2.63%, and Western Chongqing 2.47%), adding a uniform net chemical contribution to all blocks would not change the inter-block ranking. To alter the ranking, differential chemical contributions would have to exceed the observed separations, for example, φ_{chem} (Western Chongqing) − $\Delta\varphi_{\text{chem}}$ (Luzhou) > 0.16%, φ_{chem} (Changning) − φ_{chem} (Weiyuan) > 0.62%, φ_{chem} (Luzhou) − $\Delta\varphi_{\text{chem}}$ (Changning) > 0.80%. Given the broadly similar lithologic characteristics of the targeted interval and the limited fluid exchange, such pronounced differential chemical effects are considered unlikely. Therefore, the first-order conclusions, namely that compaction-driven inorganic pore loss dominates total-porosity differences and controls the inter-block trends, remain robust for the study area.

Nevertheless, this simplification defines an explicit applicability boundary: for shale reservoirs that have undergone intense chemical alteration (e.g., pervasive cementation, dissolution-driven secondary porosity, or strong open-system fluid flow), chemical diagenesis should be incorporated explicitly rather than treated as second-order. In addition, because Eq. (4) adopts an Athy-type exponential form, it should be regarded as a locally calibrated first-order compaction approximation for the LMX1 interval; shale intervals with markedly different lithofacies or stronger framework cementation may require alternative compaction formulations or recalibration.

(2) TOC–porosity intercept method (applicability boundary). The TOC–porosity intercept method provides a first-order estimate of inorganic porosity only for datasets in which TOC is the dominant control on porosity variation. Although objective screening criteria were applied, residual diagnostics against all potentially covarying factors could not be fully performed because complete mineralogical information is not available for all individual samples included in the screened well/interval datasets. Therefore, the method is most appropriate for intervals showing a clear positive

TOC–porosity relationship and should be applied with caution where burial depth, mineral composition, or formation pressure may exert strong additional controls.

(3) Limited resolution of FE-SEM for organic pores. The surface area of organic pores may be underestimated because of the limited resolution of electron microscopy. Micropores smaller than 4 nm cannot be reliably detected with conventional imaging, leading to potential underestimation of organic pore contributions. A correction method based on gas adsorption has been proposed to account for these pores (Cai et al., 2020), but it has not yet been widely applied. In addition, the P_S–R_o trend in Fig. 4 was compiled from the Wufeng–Longmaxi Formation together with published Type I–II organic-rich shale datasets from other formations to extend the maturity range. Therefore, Eq. (8) should be interpreted as a first-order empirical trend rather than a formation-independent universal law. Formation-specific depositional environment, kerogen type, and diagenetic history may introduce systematic uncertainty, particularly at the low- and high-maturity ends where Wufeng–Longmaxi data are sparse.

(4) The pressure-confined porosity correction also has limitations arising from experimental constraints. The laboratory tests simulated only overburden stress, without replicating the full complexity of in situ stress or thermal variations. As a result, the modeled evolution of restored in situ porosity may contain inaccuracies. Moreover, abnormal formation pressure data were taken from published literature rather than the specific shale gas wells studied, introducing potential discrepancies. In addition, Eq. (10) was calibrated from loading-path experiments under increasing effective stress, whereas uplift-stage porosity evolution follows an unloading path. Because shale pore recovery during unloading may be smaller owing to irreversible compaction, inelastic pore collapse, and hysteretic behavior, the modeled uplift-stage rebound of in situ porosity should be regarded as a first-order estimate and may slightly overestimate the true porosity recovery. However, because overburden stress in the study area consistently exceeds abnormal formation pressure (effective stress >30 MPa), such discrepancies are unlikely to alter the overall trend of porosity evolution, although they may affect the absolute porosity values.

6. Conclusions

For shale reservoirs in which organic matter contributes significantly to total porosity, inorganic porosity was quantified using the TOC–porosity intercept method. Considering variations in inorganic porosity and ancient burial depth across different shale gas wells, an evolution model of inorganic porosity in the Wufeng–Longmaxi shale gas reservoirs was constructed by integrating the compaction model. The organic-porosity evolution model was developed from the relationship between organic-matter surface porosity and maturity, based on ImageJ analysis of FE-SEM images. A pressure-confined porosity correction model was further established from the observed porosity–effective-stress relationships. Finally, by integrating burial history, organic-matter hydrocarbon-generation history, and formation-pressure evolution, the geological evolution of inorganic, organic, total, and in situ porosity in the Wufeng–Longmaxi shale reservoirs was reconstructed for four blocks: Luzhou, Changning, Weiyuan, and Western Chongqing.

During the rapid compaction stage and the subsequent compaction and hydrocarbon generation stage, inorganic porosity and total porosity in the four blocks decreased from ~50% to 2.47%–4.05% and 4.16%–5.76%, respectively, with increasing burial depth. Organic porosity first appeared during the compaction and hydrocarbon generation stage and increased with maturity to a maximum reconstructed value of 1.54%–1.79%. In the Luzhou block, organic porosity reached a path maximum of 1.79%, but was 1.76% at final maximum burial, suggesting only a very slight weakening of organic-pore development at the highest over-mature stage. In the uplift stage, inorganic, organic, and total porosity remained stable. After pressure-confined porosity correction, the in situ porosity at the end of the rapid compaction stage decreased to 12.13%–17.02%. During the compaction and hydrocarbon generation stage, the in situ porosity of the Changning Block continued to decrease to 2.98%. In contrast, the Luzhou, Weiyuan, and Western Chongqing blocks showed stage-wise increases but ultimately stabilized at 2.44% (Luzhou), 3.78% (Weiyuan), and 2.34% (Western Chongqing), respectively. During the uplift stage, restored in situ porosity rebounded to 2.49%–4.17%, while preserving a first-order inter-block trend among the four blocks.

Inter-block comparisons indicate that inorganic porosity is highest in Weiyuan and lowest in Western Chongqing, showing a negative correlation with maximum burial depth. The Luzhou block, which has the highest TOC, shows the highest reconstructed peak organic porosity, whereas Changning shows the lowest. However, this peak value should be understood as the maximum reached along the burial-maturation path, rather than necessarily the value attained exactly at the final maximum-burial maturity, because organic-pore development may weaken slightly at the highest over-mature stage. Because TOC and maturity differ only slightly among the four blocks, and organic porosity is relatively insensitive to maturity within $R_o \approx 2.5\%$–3.5%, the contribution of organic pores to total-porosity divergence is smaller than that of inorganic pores. Accordingly, the final total porosity largely mirrors the inorganic-porosity ranking. The proposed conceptual multi-scale model highlights effective-stress history as the first-order control and provides a framework for predicting porosity preservation and reservoir quality in deep marine shales.

CRediT authorship contribution statement

Guang-Shun Xiao: Writing – review & editing, Writing – original draft, Visualization, Validation, Supervision, Software, Resources, Project administration, Methodology, Investigation, Formal analysis, Data curation. **Neng-Wu Zhou:** Writing – review & editing, Supervision, Methodology, Funding acquisition. **Qin-Hong Hu:** Writing – review & editing, Supervision, Resources. **Sheng-Xian Zhao:** Software, Data curation. **Bo Li:** Visualization, Data curation. **Bo Song:** Data curation. **Xin-Yu Jiang:** Visualization, Data curation. **Zi-Yi Wang:** Writing – review & editing. **Shuang-Fang Lu:** Writing – review & editing, Supervision, Resources, Project administration, Methodology, Investigation, Conceptualization.

Declaration of interests

The authors declare that they have no known competing financial interests or personal relationships that could have appeared to influence the work reported in this paper.

Acknowledgements

This work was supported by the Research Project Funded by the National Natural Science Foundation of China (Grant No. 42302183).

Supplementary data

Supplementary data to this article can be found online at https://doi.org/10.1016/j.petsci.2026.06.058.

References

Anovitz, L.M., Cole, D.R., 2015. Characterization and analysis of porosity and pore structures. Rev. Mineral. Geochem. 80 (1), 61–164. https://doi.org/10.2138/rmg.2015.80.04.

Anovitz, L.M., Cole, D.R., Rother, G., et al., 2013. Diagenetic changes in macro- to nano-scale porosity in the st. Peter Sandstone: An (ultra) small angle neutron scattering and backscattered electron imaging analysis. Geochim. Cosmochim. Acta 102, 280–305. https://doi.org/10.1016/j.gca.2012.07.035.

Appelo, C.A.J., Postma, D., 2004. In: Geochemistry, Groundwater and Pollution, second ed. CRC Press, Boca Raton. https://doi.org/10.1201/9781439833544.

Athy, L.F., 1930. Density, porosity, and compaction of sedimentary rocks. AAPG Bull. 14, 1–24. https://doi.org/10.1306/3D93289E-16B1-11D7-8645000102C1865D.

Baldwin, B., Butler, C.O., 1985. Compaction curves. AAPG Bull. 69 (4), 622–626. https://doi.org/10.1306/AD462547-16F7-11D7-8645000102C1865D.

Baqer, Y., Chen, X., 2022. A review on reactive transport model and porosity evolution in the porous media. Environ. Sci. Pollut. Res. 29 (32), 47873–47901. https://doi.org/10.1007/s11356-022-20466-w.

Bei, F., Wang, Y.C., 1985. Compaction of sediment and first migration of hydrocarbon. In: Corpus of Organic Geochemistry and Continental Origin of Oil. Petroleum Industry Press, Beijing, pp. 257–264 (in Chinese).

Bello, A.M., Usman, M.B., Abubakar, U., et al., 2022. Role of diagenetic alterations on porosity evolution in the Cretaceous (Albian-Aptian) Bima Sandstone, a case study from the Northern Benue Trough, NE Nigeria. Mar. Petrol. Geol. 145, 105851. https://doi.org/10.1016/j.marpetgeo.2022.105851.

Blach, T., Radlinski, A.P., Vu, P., et al., 2021. Deformation of pores in response to uniaxial and hydrostatic stress cycling in Marcellus Shale: Implications for gas recovery. Int. J. Coal Geol. 248, 103867. https://doi.org/10.1016/j.coal.2021.103867.

Borjigin, T., Shen, B.J., Yu, L.J., et al., 2017. Mechanisms of shale gas generation and accumulation in the Ordovician Wufeng–Longmaxi Formation, Sichuan Basin, SW China. Petrol. Explor. Dev. 44 (1), 69–78. https://doi.org/10.1016/S1876-3804(17)30009-5.

Cai, X., Jin, Y.X., Ye, J.G., et al., 2020. A quantitative characterization method for organic and inorganic pores in shale. Reserv. Eval. Dev. 10 (1), 30–36. https://doi.org/10.13809/j.cnki.cn32-1825/te.2020.01.005 (in Chinese).

Cao, T.T., Deng, M., Cao, Q.G., et al., 2021. Pore formation and evolution of organic-rich shale during the entire hydrocarbon generation process: Examination of artificially and naturally matured samples. J. Nat. Gas Sci. Eng. 93, 104020. https://doi.org/10.1016/j.jngse.2021.104020.

Chen, F.J., Tian, S.C., 1989. Compaction and Hydrocarbon Migration. China University of Geosciences Press, Wuhan, pp. 113–134 (in Chinese).

Chen, F.W., Lu, S.F., Ding, X., 2014. Organoporosity evaluation of shale: A case study of the Lower Silurian Longmaxi Shale in Southeast Chongqing, China. Sci. World J. 2014, 893520. https://doi.org/10.1155/2014/893520.

Chen, J., Xiao, X.M., 2014. Evolution of nanoporosity in organic-rich shales during thermal maturation. Fuel 129, 173–181. https://doi.org/10.1016/j.fuel.2014.03.058.

Chen, Q.Q., Tang, X., Shi, Y., et al., 2025. Nanomechanics and pore structure evolution in organic-rich shale reservoirs during high-temperature treatment: A multi-scale analysis of microscopic stability. Adv. Geo-Energy Res. 17 (3), 241–255. https://doi.org/10.46690/ager.2025.09.06.

Chen, S.B., Zhu, Y.M., Wang, H.Y., et al., 2012. Structure characteristics and accumulation significance of nanopores in Longmaxi Shale gas reservoir in the southern Sichuan Basin. J. China Coal Soc. 37 (3), 438–444. https://doi.org/10.13225/j.cnki.jccs.2012.03.007 (in Chinese).

Chen, Y.C., Lin, W., Chen, Y., et al., 2024. Depositional model and controlling factors of high-quality shales of the Wufeng and Longmaxi Formations in western Chongqing, Sichuan Basin, China. ACS Omega 9 (14), 16411–16419. https://doi.org/10.1021/acsomega.4c00054.

Chen, Z.H., Jiang, C.Q., 2016. A revised method for organic porosity estimation in shale reservoirs using Rock-Eval data: Example from Duvernay Formation in the Western Canada Sedimentary Basin. AAPG Bull. 100 (3), 405–422. https://doi.org/10.1306/08261514173.

Curtis, M.E., Cardott, B.J., Sondergeld, C.H., et al., 2012. Development of organic porosity in the Woodford Shale with increasing thermal maturity. Int. J. Coal Geol. 103, 26–31. https://doi.org/10.1016/j.coal.2012.08.004.

Dewhurst, D.N., Yang, Y., Aplin, A.C., 1999. Permeability and fluid flow in natural mudstones. Geol. Soc. Lond. Spec. Publ. 158 (1), 23–43. https://doi.org/10.1144/GSL.SP.1999.158.01.03.

Dong, J.B., Ning, Y., Yi, J., et al., 2026. A novel construction approach for the pore structure model principally focuses on the controllable roundness of rock particles. Deep Undergr. Sci. Eng. 5 (1), 207–219. https://doi.org/10.1002/dug2.12151.

Dzevanshir, R.D., Buryakovskiy, L.A., Chilingarian, G.V., 1986. Simple quantitative evaluation of porosity of argillaceous sediments at various depths of burial. Sediment. Geol. 46 (3–4), 169–175. https://doi.org/10.1016/0037-0738(86)90057-6.

Emmanuel, S., Ague, J.J., Walderhaug, O., 2010. Interfacial energy effects and the evolution of pore size distributions during quartz precipitation in sandstone. Geochim. Cosmochim. Acta 74 (12), 3539–3552. https://doi.org/10.1016/j.gca.2010.03.019.

Emmanuel, S., Anovitz, L.M., Day-Stirrat, R.J., 2015. Effects of coupled chemo-mechanical processes on the evolution of pore-size distributions in geological media. Rev. Mineral. Geochem. 80 (1), 45–60. https://doi.org/10.2138/rmg.2015.03.

Giles, M.R., Indrelid, S.L., James, D.M.D., 1998. Compaction—The great unknown in basin modelling. Geol. Soc. Lond. Spec. Publ. 141 (1), 15–43. https://doi.org/10.1144/GSL.SP.1998.141.01.02.

Guo, J.L., Jia, C.Y., He, D.B., et al., 2020. Classified evaluation of shale reservoirs in the Ordovician Wufeng to Silurian Longmaxi Formations in the southern Sichuan Basin. Geol. J. China Univ. 26 (3), 323–332. https://doi.org/10.16108/j.issn1006-7493.2019047 (in Chinese).

Guo, Q.L., Chen, X.M., Song, H.Q., et al., 2013. Evolution and models of shale porosity during burial process. Nat. Gas Geosci. 24 (3), 439–449 (in Chinese).

Guo, Q.L., Wu, N., Ren, H.J., et al., 2017. Prediction models of organic pores in shale with low to moderate maturity. Lit. Res. 29 (6), 1–7. https://doi.org/10.3969/j.issn.1673-8926.2017.06.001 (in Chinese).

Guo, S.B., Mao, W.J., 2019. Division of diagenesis and pore evolution of a Permian Shanxi shale in the Ordos Basin, China. J. Petrol. Sci. Eng. 182, 106351. https://doi.org/10.1016/j.petrol.2019.106351.

Guo, Y.H., Li, Z.F., Li, D.H., et al., 2004. Lithofacies palaeogeography of the early Silurian in Sichuan area. J. Palaeogeogr. 6 (1), 20–29. https://doi.org/10.3969/j.issn.1671-1505.2004.01.003 (in Chinese).

Hao, F., Guo, T.L., Zhu, Y.M., et al., 2008. Evidence for multiple stages of oil cracking and thermochemical sulfate reduction in the Puguang gas field, Sichuan Basin, China. AAPG Bull. 92 (5), 611–637. https://doi.org/10.1306/01210807090.

Hedberg, H.D., 1936. Gravitational compaction of clays and shales. Am. J. Sci. s5–31 (184), 241–287. https://doi.org/10.2475/ajs.s5-31.184.241.

Hegarty, K.A., Weissel, J.K., Mutter, J.C., 1988. Subsidence history of Australia's southern margin: Constraints on basin models. AAPG Bull. 72 (5), 615–633. https://doi.org/10.1306/703C8EDE-1707-11D7-8645000102C1865D.

Hommel, J., Coltman, E., Class, H., 2018. Porosity–permeability relations for evolving pore space: A review with a focus on (bio-) geochemically altered porous media. Transp. Porous Medium. 124 (2), 589–629. https://doi.org/10.1007/s11242-018-1086-2.

Hou, Y., Zhang, K.P., Wang, F.R., et al., 2019. Structural evolution of organic matter and implications for graphitization in over-mature marine shales. South China. Mar. Petrol. Geol. 109, 304–316. https://doi.org/10.1016/j.marpetgeo.2019.06.009.

Hu, C.E., Tan, J.Q., Lyu, Q., et al., 2024. Evolution of organic pores in Permian low maturity shales from the Dalong Formation in the Sichuan Basin: Insights from a thermal simulation experiment. Gas Sci. Eng. 121, 205166. https://doi.org/10.1016/j.jgsce.2023.205166.

Huang, J.L., Zou, C.N., Li, J.Z., et al., 2012. Shale gas generation and potential of the Lower Cambrian Qiongzhusi formation in the southern Sichuan Basin, China. Petrol. Explor. Dev. 39 (1), 75–81. https://doi.org/10.1016/S1876-3804(12)60017-2.

Huang, Y.Z., Wang, E.Z., 2007. Experimental study on coefficient of sensitiveness between percolation rate and effective pressure for low permeability rock. Chin. J. Rock Mech. Eng. 26 (2), 410–414. https://doi.org/10.3321/j.issn:1000-6915.2007.02.025 (in Chinese).

Jarvie, D.M., Hill, R.J., Ruble, T.E., et al., 2007. Unconventional shale-gas systems: The Mississippian Barnett Shale of north-central Texas as one model for thermogenic shale-gas assessment. AAPG Bull. 91 (4), 475–499. https://doi.org/10.1306/12190606068.

Jin, Z.J., Nie, H.K., Liu, Q.Y., et al., 2018. Source and seal coupling mechanism for shale gas enrichment in the Upper Ordovician Wufeng Formation–lower Silurian Longmaxi Formation in Sichuan Basin and its periphery. Mar. Petrol. Geol. 97, 78–93. https://doi.org/10.1016/j.marpetgeo.2018.06.009.

Korvin, G., 1984. Shale compaction and statistical physics. Geophys. J. Int. 78 (1), 35–50. https://doi.org/10.1111/j.1365-246X.1984.tb06470.x.

Kuila, U., McCarty, D.K., Derkowski, A., et al., 2014. Nano-scale texture and porosity of organic matter and clay minerals in organic-rich mudrocks. Fuel 135, 359–373. https://doi.org/10.1016/j.fuel.2014.06.036.

Lin, Z.Z., Hu, Q.H., Yin, N., et al., 2026. Organic and inorganic pore networks in medium- to low-maturity shale: Insights from SEM analysis of Shahejie Formation in the Dongying Sag. Pet. Sci. 23 (1), 69–83. https://doi.org/10.1016/j.petsci.2025.09.018.

Lin, Z.Z., Li, J.Q., Lu, S.F., et al., 2024. The occurrence characteristics of oil in shale matrix from organic geochemical screening data and pore structure properties: An experimental study. Pet. Sci. 21 (1), 1–13. https://doi.org/10.1016/j.petsci.2023.09.002.

Loucks, R.G., Reed, R.M., Ruppel, S.C., et al., 2009. Morphology, genesis, and distribution of nanometer-scale pores in siliceous mudstones of the Mississippian Barnett Shale. J. Sediment. Res. 79 (12), 848–861. https://doi.org/10.2110/jsr.2009.092.

Loucks, R.G., Reed, R.M., Ruppel, S.C., et al., 2012. Spectrum of pore types and networks in mudrocks and a descriptive classification for matrix-related mudrock pores. AAPG Bull. 96 (6), 1071–1098. https://doi.org/10.1306/08171111061.

Ma, X.H., Xie, J., Yong, R., et al., 2020. Geological characteristics and high production control factors of shale gas reservoirs in Silurian Longmaxi Formation, southern Sichuan Basin, SW China. Petrol. Explor. Dev. 47 (5), 901–915. https://doi.org/10.1016/S1876-3804(20)60105-7.

Ma, X.H., Zhang, X.W., Xiong, W., et al., 2023. Prospects and challenges of shale gas development in China. Pet. Sci. Bull. 4, 491–501. https://doi.org/10.3969/j.issn.2096-1693.2023.04.037 (in Chinese).

Mathia, E.J., Bowen, L., Thomas, K.M., et al., 2016. Evolution of porosity and pore types in organic-rich, calcareous, Lower Toarcian Posidonia Shale. Mar. Petrol. Geol. 75, 117–139. https://doi.org/10.1016/j.marpetgeo.2016.04.009.

Miao, H., Jiang, Z.X., Tang, X.L., et al., 2023. Strata uplift controlled deep shale gas accumulation modes: A case study from the Weiyuan Block, Sichuan Basin. Energy Fuels 37 (17), 12889–12904. https://doi.org/10.1021/acs.energyfuels.3c02255.

Milliken, K.L., Rudnicki, M., Awwiller, D.N., et al., 2013. Organic matter-hosted pore system, Marcellus Formation (Devonian), Pennsylvania. AAPG Bull. 97 (2), 177–200. https://doi.org/10.1306/07231212048.

Mou, C.L., Ge, X.Y., Xu, X.S., et al., 2014. Lithofacies palaeogeography of the Late Ordovician and its petroleum geological significance in Middle-Upper Yangtze Region. J. Palaeogeogr. 16 (4), 427–440. https://doi.org/10.7605/gdlxb.2014.04.036 (in Chinese).

Mu, Y., Zou, C.N., Hu, Z.M., et al., 2025. Impacts of multi-scale water-rock interaction on mineral alteration, mechanical weakening and pore-fracture evolution in marine shales. Adv. Geo-Energy Res. 17 (1), 68–81. https://doi.org/10.46690/ager.2025.07.06.

Navarre-Sitchler, A., Steefel, C.I., Yang, L., et al., 2009. Evolution of porosity and diffusivity associated with chemical weathering of a basalt clast. J. Geophys. Res. 114 (F2), 2008JF001060. https://doi.org/10.1029/2008JF001060.

Neuhoff, P.S., Fridriksson, T., Arnorsson, S., et al., 1999. Porosity evolution and mineral paragenesis during low-grade metamorphism of basaltic lavas at Teigarhorn, eastern Iceland. Am. J. Sci. 299 (6), 467–501. https://doi.org/10.2475/ajs.299.6.467.

Neuzil, C.E., 1994. How permeable are clays and shales? Water Resour. Res. 30 (2), 145–150. https://doi.org/10.1029/93WR02930.

Nie, Z., Heng, D., Zou, Y.H., et al., 2021. Evolution of adsorbed gas content of marine shale in Changning area, Sichuan Basin: A case of Wufeng Formation–Longmaxi Member 1 in Well N201. Mar. Origin Petrol. Geol. 26 (1), 43–50. https://doi.org/10.3969/j.issn.1672-9854.2021.01.005 (in Chinese).

Pommer, M., Milliken, K., 2015. Pore types and pore-size distributions across thermal maturity, Eagle Ford Formation, southern Texas. AAPG Bull. 99 (9), 1713–1744. https://doi.org/10.1306/03051514151.

Puttiwongrak, A., Giao, P.H., Vann, S., 2020. An easily used mathematical model of porosity change with depth and geologic time in deep shale compaction. Int. J. GEOMATE 19 (73), 108–115. https://doi.org/10.21660/2020.73.39179.

Sang, Q., Li, Y.J., Yang, Z.H., et al., 2016. Experimental investigation of gas production processes in shale. Int. J. Coal Geol. 159, 30–47. https://doi.org/10.1016/j.coal.2016.03.017.

Sclater, J.G., Christie, P.A.F., 1980. Continental stretching: An explanation of the Post-Mid-Cretaceous subsidence of the central North Sea Basin. J. Geophys. Res. 85 (B7), 3711–3739. https://doi.org/10.1029/JB085iB07p03711.

Shi, S.Y., Wang, Y.P., Chen, C.S., et al., 2024. Influence of tectonic evolution processes on burial, thermal maturation and gas generation histories of the Wufeng–Longmaxi shale in the Sichuan Basin and adjacent areas. Int. J. Coal Geol. 295, 104642. https://doi.org/10.1016/j.coal.2024.104642.

Stack, A.G., Fernandez-Martinez, A., Allard, L.F., et al., 2014. Pore-size-dependent calcium carbonate precipitation controlled by surface chemistry. Environ. Sci. Technol. 48 (11), 6177–6183. https://doi.org/10.1021/es405574a.

Sun, S.S., Shi, Z.S., Dong, D.Z., et al., 2024. Formation and evolution of shale overpressure in deep Wufeng–Longmaxi Formation in southern Sichuan Basin and its influence on reservoir pore characteristics. Front. Earth Sci. 12, 1375241. https://doi.org/10.3389/feart.2024.1375241.

Tang, X.L., Jiang, Z.X., Jiang, S., et al., 2021. Structure, burial, and gas accumulation mechanisms of lower Silurian Longmaxi Formation shale gas reservoirs in the Sichuan Basin (China) and its periphery. AAPG Bull. 105 (12), 2425–2447. https://doi.org/10.1306/0702211610418010.

Tang, Y., Li, C.X., Cheng, H., et al., 2025. Effects of organic-inorganic transformation and interaction on the occurrence of nanopores within the organic-rich shale during thermal maturation: Insights from the hydrous pyrolysis experiments in a closed system. Pet. Sci. 22 (5), 1823–1838. https://doi.org/10.1016/j.petsci.2025.02.024.

Underdown, R., Redfern, J., 2008. Petroleum generation and migration in the Ghadames Basin, North Africa: A two-dimensional basin-modeling study. AAPG Bull. 92 (1), 53–76. https://doi.org/10.1306/08130706032.

Wang, K., Yan, W., Feng, M.G., et al., 2017. A correction method for full-diameter samples and overburden pressure of shale reservoirs: A case study of the Wufeng and Longmaxi formations in the Jiaoshiba shale gas field. Sci. Technol. Eng. 17 (21), 228–232 (in Chinese).

Wang, T., Yang, K.M., Xiong, L., et al., 2015a. Shale sequence stratigraphy of Wufeng–Longmaxi Formation in southern Sichuan and their control on reservoirs. Acta Pet. Sin. 36 (8), 915–925. https://doi.org/10.7623/syxb201508003 (in Chinese).

Wang, Y.M., Dong, D.Z., Li, J.Z., et al., 2012. Reservoir characteristics of shale gas in Longmaxi Formation of the Lower Silurian, southern Sichuan. Acta Pet. Sin. 33 (4), 551–561. https://doi.org/10.7623/syxb201204003 (in Chinese).

Wang, Y.M., Dong, D.Z., Yang, H., et al., 2014. Quantitative characterization of reservoir space in the Lower Silurian Longmaxi Shale, southern Sichuan, China. Sci. China Earth Sci. 57 (2), 313–322. https://doi.org/10.1007/s11430-013-4645-y.

Wang, Y.M., Huang, J.L., Li, X.J., et al., 2015b. Quantitative characterization of fractures and pores in shale beds of the Lower Silurian, Longmaxi Formation, Sichuan Basin. Nat. Gas Ind. B 2 (6), 481–488. https://doi.org/10.1016/j.ngib.2015.12.002.

Wang, Z.Y., Lu, S.F., Zhou, N.W., et al., 2024. Complementary testing and machine learning techniques for the characterization and prediction of Middle Permian tight gas sandstone reservoir quality in the northeastern Ordos Basin, China. Pet. Sci. 21 (5), 2946–2968. https://doi.org/10.1016/j.petsci.2024.08.008.

Wu, J., Chen, X.Z., Liu, W.P., et al., 2022. Fluid activity and pressure evolution process of Wufeng–Longmaxi shales, southern Sichuan Basin. Earth Sci. 47 (2), 518–531. https://doi.org/10.3799/dqkx.2021.049 (in Chinese).

Wu, Y.H., Lu, S.F., Chen, F.W., et al., 2015. Quantitative characterization of organic pores in muddy shale reservoirs. Special Oil Gas Reservoirs 22 (5), 65–68. https://doi.org/10.3969/j.issn.1006-6535.2015.05.013 (in Chinese).

Xiao, X.M., Wang, M.L., Wei, Q., et al., 2015. Evaluation of Lower Paleozoic shale with shale gas prospect in South China. Nat. Gas Geosci. 26 (8), 1433–1445. https://doi.org/10.11764/j.issn.1672-1926.2015.08.1433 (in Chinese).

Xie, X.M., Volkman, J.K., Qin, J.Z., et al., 2014. Petrology and hydrocarbon potential of microalgal and macroalgal dominated oil shales from the Eocene Huadian Formation, NE China. Int. J. Coal Geol. 124, 36–47. https://doi.org/10.1016/j.coal.2013.12.013.

Xu, X.M., Zhang, X.T., Shen, B., et al., 2025. Formation and development of pore structure in transitional shale—insights from thermal simulation experiments on the Shanxi Formation Shale in the Ordos Basin. ACS Omega 10 (21), 21963–21979. https://doi.org/10.1021/acsomega.5c01831.

Yang, B.G., Pan, R.F., Liu, L., et al., 2015. The influence of geological conditions in the changning demonstration area, Sichuan Basin, on the development of organic matter in shale. Sci. Technol. Eng. 15 (26), 35–41 (in Chinese).

Yang, W., Wang, Y.H., Du, W., et al., 2022. Behavior of organic matter-hosted pores within shale gas reservoirs in response to differential tectonic deformation: Potential mechanisms and innovative conceptual models. J. Nat. Gas Sci. Eng. 102, 104571. https://doi.org/10.1016/j.jngse.2022.104571.

Yang, W., Yang, R., Wang, M., et al., 2025. Impact of lithofacies categories on inflection-point behaviors in micro-nano pore-structure evolution: Implications for differential reservoir-forming mechanisms and "sweet-spot intervals" identification for marine gas shales. Mar. Petrol. Geol. 176, 107336. https://doi.org/10.1016/j.marpetgeo.2025.107336.

Yang, X.G., Guo, S.B., 2020a. Pore characterization of marine-continental transitional shale in Permian Shanxi Formation of the southern North China Basin. Energy Explor. Exploit. 38 (6), 2199–2216. https://doi.org/10.1177/0144598720912346.

Yang, X.G., Guo, S.B., 2020b. Porosity model and pore evolution of transitional shales: an example from the southern North China Basin. Pet. Sci. 17 (6), 1512–1526. https://doi.org/10.1007/s12182-020-00481-7.

Yu, W.M., Tang, H.M., 2019. Experimental study on the existence of nano-scale pores and the evolution of organic matter in organic-rich shale. Nanotechnol. Rev. 8 (1), 156–167. https://doi.org/10.1515/ntrev-2019-0015.

Zhang, B., Wen, H., Qing, H., et al., 2022. The influence of depositional and diagenetic processes on rock electrical properties: A case study of the Longmaxi shale in the Sichuan Basin. J. Petrol. Sci. Eng. 211, 110119. https://doi.org/10.1016/j.petrol.2022.110119.

Zhang, B.Q., Guan, Z.L., Zhang, G.Y., 1992. Application of Compaction in the Exploration of Oil. China University of Geosciences Press, Wuhan (in Chinese).

Zhang, G.Y., Fu, Q., Peng, G.G., et al., 2023. Diagenetic evolution and petrophysical characteristics of Paleogene sandstone reservoirs in the southwest Baiyun Sag, northern South China Sea. Minerals 13 (10), 1265. https://doi.org/10.3390/min13101265.

Zhang, Q., Yue, X.J., 2021. Experimental study on porosity and permeability and stress sensitivity of shale under pressurization. Geol. Bull. China 40 (9), 1514–1521. https://doi.org/10.12097/gbc.dztb-40-9-1514 (in Chinese).

Zhang, S.R., Dong, D.Z., Liao, Q.S., et al., 2021. Geological characteristics and resource prospect of deep marine shale gas in the southern Sichuan Basin. Nat. Gas. Ind. 41 (9), 35–45. https://doi.org/10.3787/j.issn.1000-0976.2021.09.004 (in Chinese).

Zhang, Y., Liu, L., 2021. Insights into the formation mechanism of low water saturation in Longmaxi Shale in the Jiaoshiba area, eastern Sichuan Basin. J. Earth Sci. 32 (4), 863–871. https://doi.org/10.1007/s12583-020-1353-3.

Zhang, Y., Zhao, P.R., Gao, S.L., et al., 2025. Practice and enlightenment of high-quality shale oil and gas exploration of Sinopec. China Petrol. Explor 30 (1), 16–27. https://doi.org/10.3969/j.issn.1672-7703.2025.01.002 (in Chinese).

Zhao, W.Z., Li, J.Z., Yang, T., et al., 2016. Geological difference and its significance of marine shale gases in South China. Petrol. Explor. Dev. 43 (4), 547–559. https://doi.org/10.1016/S1876-3804(16)30065-9.

Zhou, N.W., Wang, M., Lu, S.F., et al., 2023. Evolution of pore space in tight sandstone: The roles of dissolution, calcite cementation, and clay growth. AAPG Bull. 107 (9), 1609–1635. https://doi.org/10.1306/12202221020.

Zhou, Y., Zhong, X.Q., Nie, X., 2024. Identification and parameter characterization of pores and fractures in shales based on multi-scale digital core data. Adv. Geo-Energy Res. 13 (2), 146–160. https://doi.org/10.46690/ager.2024.08.08.

Zou, C., Dong, D., Wang, S., et al., 2010. Geological characteristics and resource potential of shale gas in China. Petrol. Explor. Dev. 37 (6), 641–653. https://doi.org/10.1016/s1876-3804(11)60001-3.